

FIRST SPECTROSCOPIC EVIDENCE FOR HIGH IONIZATION STATE AND LOW OXYGEN ABUNDANCE IN LY α EMITTERS ^{† ‡}

KIMIHIKO NAKAJIMA ^{1,3}, MASAMI OUCHI ^{2,3}, KAZUHIRO SHIMASAKU ^{1,4}, TAKUYA HASHIMOTO ¹, YOSHIAKI ONO ^{1,2},
AND JANICE C. LEE ^{5,6,7,8}

Accepted for publication in ApJ

ABSTRACT

We present results from Keck/NIRSPEC and Magellan/MMIRS follow-up spectroscopy of Ly α emitters (LAEs) at $z = 2.2$ identified in our Subaru narrowband survey. We successfully detect H α emission from seven LAEs, and perform a detailed analysis of six LAEs free from AGN activity, two out of which, CDFS-3865 and COSMOS-30679, have [O II] and [O III] line detections. They are the first [O II]-detected LAEs at high- z , and their [O III]/[O II] ratios and $R23$ -indices provide the first simultaneous determinations of ionization parameter and oxygen abundance for LAEs. CDFS-3865 has a very high ionization parameter ($q_{ion} = 2.5^{+1.7}_{-0.8} \times 10^8 \text{ cm s}^{-1}$) and a low oxygen abundance ($12 + \log(\text{O}/\text{H}) = 7.84^{+0.24}_{-0.25}$) in contrast with moderate values of other high- z galaxies such as Lyman-break galaxies (LBGs). COSMOS-30679 also possesses a relatively high ionization parameter ($q_{ion} = 8^{+10}_{-4} \times 10^7 \text{ cm s}^{-1}$) and a low oxygen abundance ($12 + \log(\text{O}/\text{H}) = 8.18^{+0.28}_{-0.28}$). Both LAEs appear to fall below the mass-metallicity relation of $z \sim 2$ LBGs. Similarly, a low metallicity of $12 + \log(\text{O}/\text{H}) < 8.4$ is independently indicated for typical LAEs from a composite spectrum and the [N II]/H α index. Such high ionization parameters and low oxygen abundances can be found in local star-forming galaxies, but this extreme local population occupies only $\sim 0.06\%$ of the SDSS spectroscopic galaxy sample with a number density ~ 100 times smaller than that of LAEs. With their high ionization parameters and low oxygen abundances, LAEs would represent an early stage of galaxy formation dominated by massive stars in compact star-forming regions. High- q_{ion} galaxies like LAEs would produce ionizing photons efficiently with a high escape fraction achieved by density-bounded HII regions, which would significantly contribute to cosmic reionization at $z > 6$.

Subject headings: galaxies: evolution

1. INTRODUCTION

Ly α emitters (LAEs), galaxies commonly observed at high redshifts with strong Ly α emission, are considered to be low-mass, young galaxies as suggested from their small sizes, faint continua, and low masses inferred from spectral energy distribution (SED) fitting (e.g., Venemans et al. 2005; Gawiser et al. 2006; Pirzkal et al. 2007; Overzier et al. 2008; Malhotra et al. 2012). LAEs

are therefore likely to represent galaxies in the early stages of galaxy evolution. More directly, Cowie et al. (2011) investigate rest-frame optical nebular lines of LAEs at low redshifts ($z \sim 0.3$). The authors find that a large portion of LAEs (75%) have equivalent width (EW) of H $\alpha > 100 \text{ \AA}$, and that LAEs on average have lower metallicities and younger ages than the UV-continuum sample. These findings are consistent with the idea that LAEs are galaxies in early stages of galaxy formation. At higher redshifts, LAEs are efficiently detected thanks to narrowband imaging techniques which have enriched our knowledge about the younger universe (e.g., Cowie & Hu 1998; Malhotra & Rhoads 2002; Ouchi et al. 2003; Gawiser et al. 2006; Shimasaku et al. 2006; Gawiser et al. 2007; Gronwall et al. 2007; Ouchi et al. 2008; Nilsson et al. 2009; Guaita et al. 2010; Finkelstein et al. 2011; Nakajima et al. 2012). However, more direct evidence supporting the idea that high redshift LAEs are in an early evolutionary phase of formation is still needed.

The gas-phase metallicity is a key property of galaxies, since it is a record of their star-formation histories. This physical quantity is relatively easily constrained with line ratios of nebular lines at rest-frame optical wavelengths (e.g., Pagel et al. 1979; Kewley & Dopita 2002, and references therein). Another key quantity is the ionization parameter, defined as the ratio of the mean ionizing photon flux to the mean hydrogen atom density. Since the excitation of the HII region is sensitive to the

nakajima@astron.s.u-tokyo.ac.jp

¹ Department of Astronomy, Graduate School of Science, The University of Tokyo, 7-3-1 Hongo, Bunkyo-ku, Tokyo 113-0033, Japan

² Institute for Cosmic Ray Research, The University of Tokyo, 5-1-5 Kashiwanoha, Kashiwa, Chiba 277-8582, Japan

³ Kavli Institute for the Physics and Mathematics of the Universe (WPI), The University of Tokyo, 5-1-5 Kashiwanoha, Kashiwa, Chiba 277-8583, Japan

⁴ Research Center for the Early Universe, Graduate School of Science, The University of Tokyo, Tokyo 113-0033, Japan

⁵ Space Telescope Science Institute, Baltimore, MD, USA

⁶ Visiting Astronomer, SSC/IPAC, Caltech, Pasadena, CA, USA

⁷ Observatories of the Carnegie Institution of Washington, 813 Santa Barbara Street, Pasadena, CA 91101, USA

⁸ Carnegie Fellow

[†] Some of the data presented herein were obtained at the W.M. Keck Observatory, which is operated as a scientific partnership among the California Institute of Technology, the University of California and the National Aeronautics and Space Administration. The Observatory was made possible by the generous financial support of the W.M. Keck Foundation.

[‡] Based in part on data collected at Subaru Telescope, which is operated by the National Astronomical Observatory of Japan.

age distribution of the exciting stars, the ionization parameter provides a rough estimate of age of a galaxy (e.g., Dopita et al. 2006). A large ionization parameter is observed from a galaxy dominated with massive stars, which is a sign that the galaxy is in an early stage of galaxy formation. In addition, the ionization parameter depends on the optical depth in an HII region (e.g., Brinchmann et al. 2008); a large ionization parameter may be instead due to a low optical depth and a high escape fraction of ionizing photons. Therefore, constraining ionization parameters for LAEs may provide an independent clue to whether or not LAEs, commonly observed star-forming galaxies at high redshift, significantly contribute to the cosmic reionization in the early universe. Determining the ionization parameter requires two emission lines of different ionization stages of a same element, such as [O II] and [O III] (e.g., Kewley & Dopita 2002).

However, well-defined samples of LAEs are generally located at very high redshifts ($3 < z < 7$), where rest-frame optical nebular lines are redshifted into infrared wavelengths. Recently, Finkelstein et al. (2011) and Nakajima et al. (2012) instead take advantage of LAEs at moderately high redshifts ($z \sim 2$), where the nebular lines up to H α are observable from the ground in the near-infrared (NIR) windows.

These studies extend the metallicity censuses to galaxies with strong Ly α emission. Finkelstein et al. (2011) obtain NIR spectra for two $z \sim 2.4$ LAEs, and find that at least one LAE appears to be less chemically enriched than $z \sim 2$ continuum-selected galaxies at similar stellar masses (Erb et al. 2006a). Nakajima et al. (2012) estimate average line fluxes for [O II] λ 3727 and H α + [N II] λ 6584 for $z = 2.2$ LAEs by stacking 1.18 and 2.09 μ m narrowband images for more than 100 LAEs, and place a firm lower-limit for the average metallicity of this population. Interestingly, the lower-limit is higher than expected for its stellar mass at the redshift.

In contrast to the gas-phase metallicities, the ionization parameters of LAEs are unknown. Such measurements have only been obtained for bright galaxies such as Lyman-break galaxies (LBGs) or strongly lensed galaxies at high- z (e.g., Pettini et al. 2001; Hainline et al. 2009; Richard et al. 2011). Although the current number of measurements is small, ionization parameters of such high- z galaxies are likely to be higher on average than those of local galaxies. A comparison of ionization parameters for LBGs and LAEs will enable us to discuss whether or not LAEs are young galaxies at high redshifts.

In order to obtain reliable measurements of properties including metallicity and ionization parameter of LAEs at high redshifts, we have carried out a large survey for $z = 2.2$ LAEs, using our custom narrowband filter NB387 with Subaru/Suprime-Cam. At $z = 2.2$, important nebular lines such as [O II] λ 3727, H β , [O III] λ 5007, 4959, H α , [N II] λ 6584, are observable from the ground. Initial results were based on using three narrowbands to detect Ly α , [O II], and H α over the same volumes (Nakajima et al. 2012; see also Lee et al. 2012 and Ly et al. 2011 for the two NIR narrowbands and the NewH α Survey).

In this paper, we present results from NIR spectroscopy. We used Keck/NIRSPEC and Magel-

lan/MMIRS spectrographs, and successfully detected H α emission from seven LAEs. The number is double the previous number of high- z LAEs with NIR spectra (two from Finkelstein et al. 2011 and two from McLinden et al. 2011), and allows us to begin to examine statistical variation of rest-frame optical spectroscopic properties of LAEs at $z \sim 2$. Our first NIR spectroscopic result discusses the kinematics of LAEs and is presented in Hashimoto et al. (2013). As a companion study, this paper presents the ionization and chemical properties of LAEs based on multiple nebular lines. Remarkably, we detected [O II] and [O III] lines from two LAEs, which provide ionization parameter estimates for LAEs for the first time. In addition, the oxygen lines allow us to determine oxygen abundances that compliment the previous spectroscopic constraints on metallicity of LAEs from the [N II]/H α index.

We also investigate Ly α and H α hydrogen lines for LAEs. A comparison of observed Ly α /H α ratios with the Case B recombination value (Ly α /H α = 8.7; Brocklehurst 1971) provides important insights into the physical mechanisms causing the strong Ly α emission in LAEs. Furthermore, we study Ly α and H α equivalent widths which probe star-formation history, stellar age, and metallicity.

This paper is organized as follows. We describe the data in §2. The detection and measurement of emission lines in the NIR spectroscopy is summarized in §3. In §4, we derive properties of LAEs including estimates of ionization parameter, metallicity, and SFR from the rest-frame optical nebular lines. We also check for the presence of active galactic nuclei (AGN) in the LAEs. In §5, we compare LAEs with other galaxies in terms of their ionization state, metallicity, and SFR. We then discuss the implications. We also discuss the physical properties inferred from Ly α and H α emission. We conclude the paper in §6 with a summary. Throughout this paper, magnitudes are given in the AB system (Oke 1974), and we assume a standard Λ CDM cosmology with $(\Omega_m, \Omega_\Lambda, H_0) = (0.3, 0.7, 70 \text{ km s}^{-1} \text{ Mpc}^{-1})$.

2. NIR SPECTROSCOPIC DATA

2.1. Sample Construction

We carried out NB387 ($\lambda_c = 3870 \text{ \AA}$ and FWHM = 94 \AA) imaging observation with Subaru/Suprime-Cam (Miyazaki et al. 2002) on 2009 December 14-16 and 19-20 to search for $z = 2.2$ LAEs. A total of ~ 1.5 square degrees are covered, with pointings in the following five fields: the Subaru/*XMM-Newton* Deep Survey (SXDS) field (Furusawa et al. 2008), the COSMOS field (Scoville et al. 2007), the Chandra Deep field South (CDFs; Giacconi et al. 2001), the Hawaii Hubble Deep Field North (HHDFN; Capak et al. 2004), and the SSA22 field (e.g., Steidel et al. 2000). The first results of the NB387 survey in the SXDS field have been presented in Nakajima et al. (2012). For the other fields, we select $z = 2.2$ LAE candidates in the same manner as presented in Nakajima et al. (2012), and a summary of the full ~ 1.5 square degrees survey will be presented elsewhere (K. Nakajima et al. in preparation). Briefly, objects which are bright in NB387 compared to the U and B bands are selected as LAE candidates. The color criterion for SXDS, COSMOS, and

TABLE 1
SUMMARY OF THE LAE SAMPLE WITH NIR SPECTROSCOPY

Object	R.A.	Decl.	NB387	$U-NB387$	$B-NB387$	$EW(Ly\alpha)$	$F(Ly\alpha)$	EXPTIME ⁽⁶⁾			Instr.
	(1)	(1)	(2)	(3)	(3)	(4)	(5)	(<i>J</i>)	(<i>H</i>)	(<i>K</i>)	(7)
COSMOS-08501	10:01:16.80	+02:05:36.26	23.94	1.41 ± 0.09	2.05 ± 0.10	255 ± 26	24.0 ± 1.1	3600	N
COSMOS-13636	09:59:59.38	+02:08:38.36	23.53	0.91 ± 0.05	1.03 ± 0.06	73 ± 5	32.4 ± 1.4	5400	N
COSMOS-30679	10:00:29.81	+02:18:49.00	23.63	0.86 ± 0.05	0.55 ± 0.06	34 ± 3	19.1 ± 1.4	5400	7200	6300	N
COSMOS-30679 ^(†)	23.73	1.20 ± 0.07	1.16 ± 0.07	87 ± 7	23.2 ± 1.8
COSMOS-43982	09:59:54.39	+02:26:29.96	23.83	1.14 ± 0.08	1.30 ± 0.07	105 ± 8	30.3 ± 1.3	3600	N
HHDFN-18325	12:36:23.36	+62:06:05.10	21.84	1.26 ± 0.02	1.50 ± 0.02	122 ± 2	$125. \pm 1.2$	3600	N
HHDFN-18431	12:36:25.62	+62:05:37.43	23.20	1.15 ± 0.03	1.71 ± 0.04	156 ± 6	37.8 ± 0.7	3600	N
CDFS-3865	03:32:32.31	-28:00:52.20	22.29	1.42 ± 1.23	1.01 ± 0.42	64 ± 29	84.0 ± 13.9	5100	10800		N/M
CDFS-6482	03:32:49.34	-27:59:52.35	23.26	1.47 ± 1.92	0.96 ± 0.66	75 ± 52	41.9 ± 22.0	...	10800		M
SSA22-8043	22:17:47.33	+00:08:28.36	24.51	0.66 ± 0.06	0.52 ± 0.06	28 ± 4	6.3 ± 1.1	...	10800		M

NOTE. — (1) Coordinates are in J2000. (2) NB387 aperture magnitude. The diameter of the aperture is $2''$, and the typical error is 0.04 mag. (3) $U-NB387$ and $B-NB387$ colors and their 1σ errors calculated from aperture magnitudes. (4) Rest-frame EW of $Ly\alpha$ emission line in units of \AA calculated from $B-NB387$ color and redshift of $H\alpha$. For HHDFN objects whose $H\alpha$ are not detected, we assume $z = 2.18$, which corresponds to the wavelength of the peak of the NB387 transmission curve. (5) Flux of $Ly\alpha$ emission line in units of $10^{-17} \text{ erg s}^{-1} \text{ cm}^{-2}$ calculated from $EW(Ly\alpha)$ and B band total magnitude. (6) Exposure time with NIRSPEC J , H , and K bands in units of second. For the CDFS and SSA22 objects, their H and K bands spectra were taken with MMIRS using the HK grism. (7) Instrument used for the spectroscopy. “N” stands for NIRSPEC, and “M” for MMIRS. For CDFS-3865, its J band spectrum was obtained with NIRSPEC, and H and K bands spectra with MMIRS. (†) Values obtained after removing the contribution from an adjacent object (§4.2).

SSA22 is $u^* - NB387 > 0.5$ & $B - NB387 > 0.2$, while $U - NB387 > 0.8$ & $B - NB387 > 0.2$ for CDFS and $U - NB387 > 0.5$ & $B - NB387 > 0.2$ for HHDFN. These criteria results in selecting objects with emission line possessing $EW_{\text{rest}} \gtrsim 30 \text{ \AA}$. The 2σ photometric errors in $u^* - NB387$ (or $U - NB387$) are additionally used as the minimum excess for an object to enter the sample. Note that this narrowband excess criterion is only significant for CDFS, where broadband data are shallow with respect to the NB387 data. Although a much deeper U-band data exist in CDFS (Nonino et al. 2009), we use the shallower U-band since it has a wider coverage¹¹. Since the U-band data is not directly used when deriving physical properties, the shallowness is not significant in this paper. Interlopers such as [O II] emitters, CIV emitters, or active galactic nuclei (AGNs) are removed from the catalog by using UV, X-ray and/or radio data.

Seven candidates were selected for NIRSPEC follow-up. We selected COSMOS-13636, COSMOS-30679, and COSMOS-43982, since their $Ly\alpha$ spectra had been obtained with Magellan/MagE (M. Rauch et al. in preparation). COSMOS-08501, HHDFN-18325, and HHDFN-18431 were selected because of their large $Ly\alpha$ equivalent widths and fluxes measured from the NB387 imaging data. CDFS-3865, whose rest-frame optical spectrum has in part already been taken with MMIRS, was also observed with NIRSPEC for its [O II] detection. Table 1 summarizes the details of the sample.

For the MMIRS observation, we observed CDFS and SSA22 fields with one mask each. Details of the observation and data reduction procedures are presented in Hashimoto et al. (2013). Briefly, we found three LAEs in which we identified $H\alpha$ emission. In this paper, we make use of the spectra of the three LAEs; CDFS-3865, CDFS-6482, and SSA22-8043 (Table 1). Figure 1 shows the distributions of the LAEs presented in this paper on the $U - NB387$ versus NB387 color magnitude diagram.

2.2. NIRSPEC Observation

The observations were carried out on 9–10 February 2011. Both nights were photometric. We observed in low-resolution mode, with a slit width of $0''.76$ and a slit length of $42''.12$. We observed all six candidate with Nirspec-6 filter (hereafter referred to as K band). In addition, we observed COSMOS-30679 with Nirspec-5 (H band) and Nirspec-3 (J band), and CDFS-3865 with J band. The wavelength ranges of K , H , and J bands are $1.88\text{--}2.31 \mu\text{m}$, $1.47\text{--}1.76 \mu\text{m}$, and $1.15\text{--}1.36 \mu\text{m}$, respectively for our configurations. The resolution in the K band is $R \sim 1500$. Exposure times for each object are given in Table 1.

Our science targets were acquired using the invisible object acquisition procedures. In this mode, an alignment star brighter than $K_{\text{Vega}} \sim 18$ was placed in the slit simultaneously with a science target. We first acquired the star at the center of the slit, then we nodded the telescope so that both the science target and the star were on the slit with the same distance from the slit center. For CDFS-3865 and HHDFN-18431, since we could not find any stars to place on the slit along with them, we first acquired the nearest star to the target (at distances of $68''$ for CDFS-3865 and $39''$ for HHDFN-18431), then nodded the telescope with an offset, which was calculated from the WCS difference between the star and the science target. For HHDFN-18325, although a star was found at a distance of $32''$, which is smaller than the slit length, half of the observation was done without the star in order to avoid the persistence caused by the previous target alignment star. During an exposure, we manually guided the slit using the slit-viewing camera; if the star started to drift out of the slit, we manually moved the slit so that the star (and thus the invisible science target) stayed in the slit throughout each exposure.

Standard stars, which were selected from the Hipparcos catalog to have A0V spectral type and similar airmass to the science targets, were observed at the beginnings and the ends of the nights. The calibration data were taken in an ABBA position pattern, while the science data in

¹¹ In addition, CDFS-3865 is located near the edge of the deeper image.

¹² The effective slit length is $\sim 38''$, since we did not place objects in $< 2''$ from the edges of the slit.

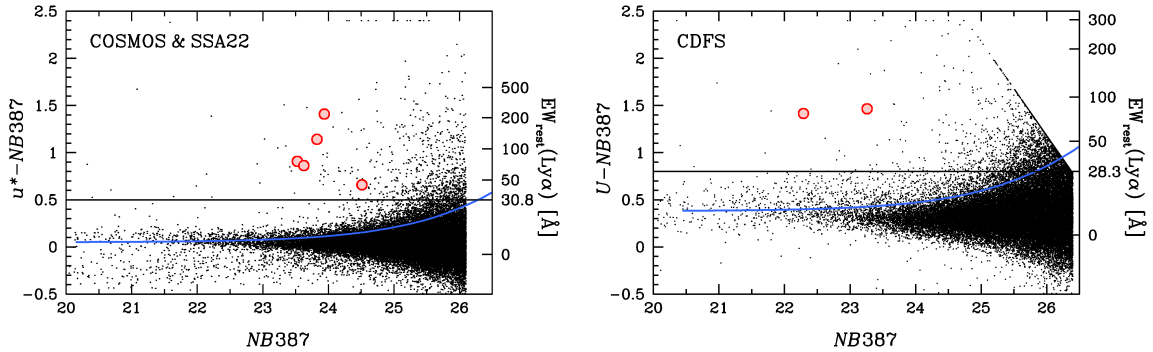


FIG. 1.— Distribution of all objects in the u^* -NB387 vs. NB387 plane detected in the COSMOS and SSA22 fields (left) and in the U -NB387 vs. NB387 plane in the CDFS field (right). The red circles show the LAEs presented in this paper, and the black dots show the NB387-detected objects. For the purpose of display, objects whose u^* -NB387 (or U -NB387) colors exceed 2.4 are plotted at u^* -NB387 (U -NB387) = 2.4. The horizontal solid line in each panel shows the selection threshold of u^* -NB387 (U -NB387) and the blue curve indicates the 2σ photometric error in u^* -NB387 (U -NB387) for objects with u^* -NB387=0.05 (U -NB387=0.38) in the COSMOS and SSA22 (CDFS) fields, which is the average color of all the objects. The right y -axis in each panel shows the rest-frame Ly α equivalent width of $z = 2.18$ LAEs with the u^* -NB387 (U -NB387) color corresponding to the left y -axis.

TABLE 2
FLUXES OF NEBULAR LINES DETERMINED FROM NIR SPECTROSCOPY

Object	[O II] λ 3727	H β	[O III] λ 4959	[O III] λ 5007	H α	[N II] λ 6484
COSMOS-08501	1.91 ± 0.36	< 0.36
COSMOS-13636	2.71 ± 0.38	< 0.38
COSMOS-30679	1.04 ± 0.26	... (†)	... (†)	4.11 ± 0.41	3.11 ± 0.27	< 0.27
COSMOS-43982	6.63 ± 0.58	4.14 ± 0.58
Composite ^(*)	2.64 ± 0.20	< 0.20
CDFS-3865	2.53 ± 0.41	13.0 ± 4.1	19.0 ± 3.5	53.6 ± 3.5	38.5 ± 2.4	< 2.4
CDFS-6482	23.8 ± 2.7	9.38 ± 1.71	< 1.71
SSA22-8043	11.0 ± 4.2	14.7 ± 4.3	< 4.3

NOTE. — Fluxes and their 1σ errors are given in unit of 10^{-17} ergs $^{-1}$ cm $^{-2}$. For lines with less than the 3σ detection level, we list their 1σ upper-limits. (*) Composite spectrum of the four objects (§4.1). (†) These lines suffer badly from OH-lines subtraction errors.

AB position pattern.

2.3. NIRSPEC Data Reduction

We used the Keck IRAF-based WMKONSPEC package¹³ to reduce the data. We also used IRAF scripts that were originally written for reducing near-infrared multi-object spectroscopic data from Subaru/MOIRCS (MCSMDP; Yoshikawa et al. 2010).

The data reduction process included bias subtraction, flat fielding, distortion correction, wavelength calibration, cosmic ray rejection, (A-B) sky subtraction, residual background subtraction, image shifting, and stacking. We used the bias and flat data that were obtained in the same night as the science data. We performed wavelength calibration using OH-lines by comparing them with an OH-line list (Rousselot et al. 2000). For cosmic ray rejection, we used *LA.COSMIC* (van Dokkum 2001). The sky and OH-lines of an A-position image were roughly removed by subtracting an average B-position image created from the previous and following images. We then removed the residual sky by subtracting a 9-th order polynomial fit in the spatial direction after masking columns of positive and negative parts caused by the alignment star and the object. Individual images were shifted in spatial direction so that the object is in

the same position both in A-position and B-position images. The offset values were derived from the position differences of the alignment stars. When no star was observed simultaneously, we defined the offset values as the nod separation size. Finally, we stacked the position-matched individual images to create the two-dimensional (2D) spectra.

We obtained flux solutions by comparing spectra of the A0V standard stars and a model, which was created by a stellar spectral synthesis program (SPECTRUM; Gray & Corbally 1994) based on the Kurucz (1993)'s atmosphere models. The model spectra were then normalized so that their J , H , and K band magnitudes matched with those of standard stars, whose photometry was obtained from the Two Micron All Sky Survey (2MASS) All-Sky Point Source Catalog. The one-dimensional (1D) spectra were extracted by summing up 6–10 pixels in the spatial direction. The lengths of columns were determined based on the seeing conditions; about two times the seeing size was used. We also confirmed that the sizes were large enough to detect most of the signal, and maximize the signal-to-noise (S/N) ratio. The 1D and 2D spectra are shown in Figure 2. We note in addition that the science targets and the standard stars used for the flux calibrations were observed and reduced with almost the same conditions, thus effects of slit losses were also corrected in the procedures, since the standard spec-

¹³ <http://www2.keck.hawaii.edu/inst/nirspec/wmkonspec.html>

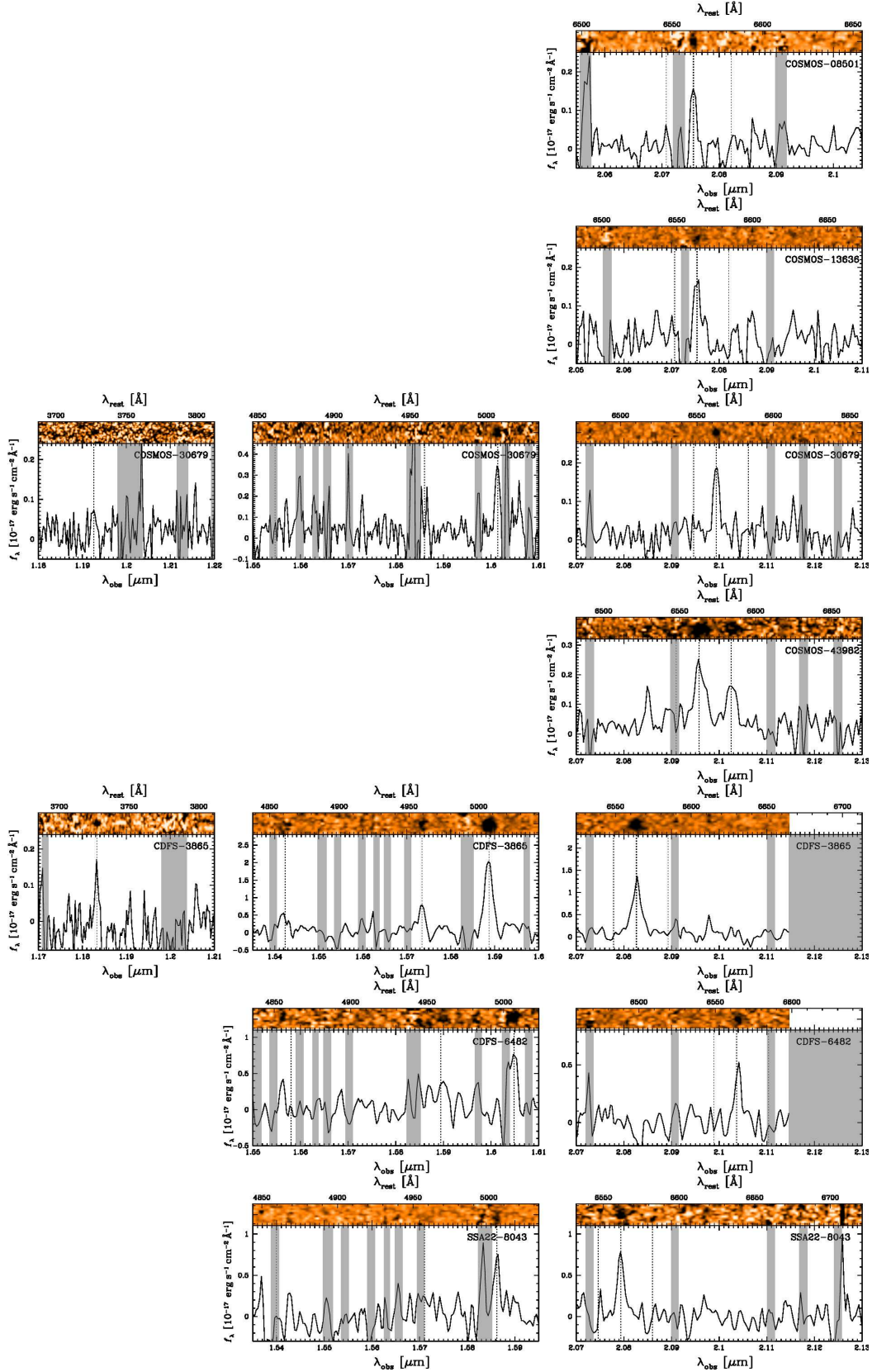


FIG. 2.— From left to right, J , H , and K band spectra of the LAEs. In each panel, the 2D and 1D spectra are shown in the top and bottom, respectively. The vertical dotted lines in the 1D spectra show the expected locations of nebular emission lines; $[\text{O III}]\lambda 3727$, $\text{H}\beta$, $[\text{O III}]\lambda 4959$, 5007 , $[\text{N II}]\lambda 6548$, $\text{H}\alpha$, and $[\text{N II}]\lambda 6584$ based on the peak of the detected $\text{H}\alpha$ emission lines. The gray shaded areas overlaid on each 1D spectrum highlight spectral regions strongly affected by OH-airglow. For CDFS objects, their K band spectra at $2.115 \mu\text{m}$ are not obtained due to a lack of sensitivity of MMIRS, and also shaded with gray.

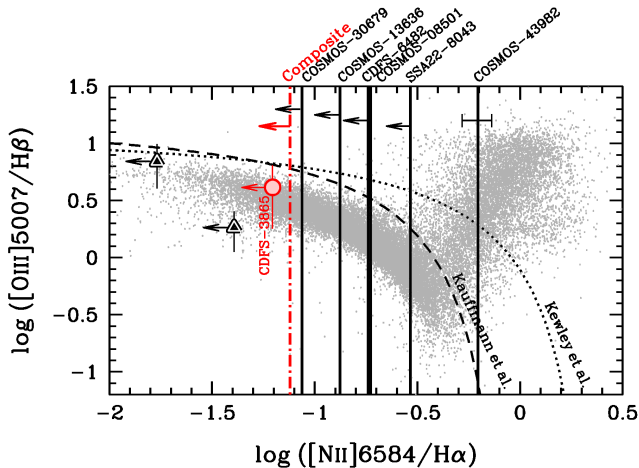


FIG. 3.— BPT-diagram (Baldwin et al. 1981). The dotted and dashed curves show the dividing line between star-forming galaxies and AGNs defined by Kewley et al. (2001) and Kauffmann et al. (2003), respectively. CDFS-3865 is shown with the red circle, while the other LAEs are shown with the vertical solid lines, due to the lacks of [O III] and/or H β . Since we do not identify [N II] except for COSMOS-43982, upper-limits of [N II]/H α are given. The [N II]/H α ratio for COSMOS-43982 is given with a horizontal error bar. The red dot-dashed vertical line indicates the upper-limit of [N II]/H α for the composite spectrum of NIRSPEC-detected LAEs. The two triangles represent LAEs at $z \sim 2.3$ and 2.5 from Finkelstein et al. (2011). The gray small points are randomly selected objects from the SDSS spectroscopic sample.

tra extracted in the procedure were normalized to have the total magnitude of that star. LAEs typically have half-light radii $\lesssim 1.5$ kpc ($\lesssim 0''.18$ at $z = 2.2$; Bond et al. 2009), which is much smaller than the seeing size. Therefore, we cannot resolve LAEs with our observations, and assuming the PSF profile for the LAEs is reasonable.

Emission line fluxes were measured by fitting a Gaussian profile to each line with the IRAF task `splot`. The sky noise level was estimated in the following manner; we prepared an aperture box, which had approximately twice the seeing size in spatial direction and twice the FWHM of the best fit Gaussian to the emission line in wavelength direction. We spread more than 100 aperture boxes around the emission line after masking pixels heavily contaminated by OH-lines, and measured their photon counts. We then fit the histogram of the counts with a Gaussian, and regarded its σ as the 1σ fluctuation for the aperture used to measure the emission line. The line fluxes and their 1σ errors are summarized in Table 2.

3. EMISSION LINE DETECTIONS

3.1. H α detection

We detect significant H α emission in K band 2D spectra for COSMOS-08501, COSMOS-13636, COSMOS-30679, COSMOS-43982, CDFS-3865, CDFS-6482, and SSA22-8043, but we do not identify any emission lines for the other two LAEs, HHDFN-18325 and HHDFN-18431. Both LAEs are expected to have strong Ly α , hence strong H α . A possible reason why we do not detect lines for HHDFN-18431 is that no alignment star was observed simultaneously, and the object may have drifted significantly out of the slit. The same issue may explain the non-detection of H α for HHDFN-18325, since half of the observation was done without an alignment star (§2.2). Since we have not yet obtained Ly α spectra

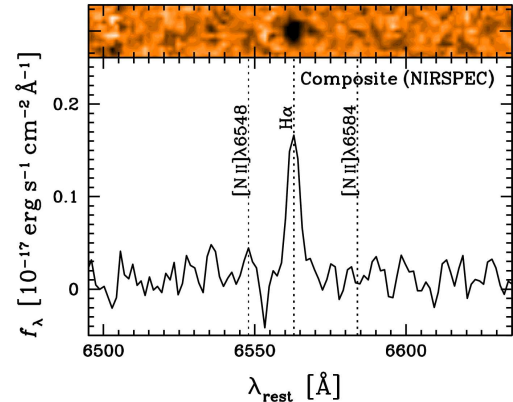


FIG. 4.— K band composite spectrum of the NIRSPEC-detected objects.

for the two objects, the non-detections may be alternatively due to the mis-selection of LAEs. Future optical spectroscopy is needed to resolve this issue. In the following sections, we use the seven LAEs with reliable H α detection.

3.2. Other emission line detections

For CDFS-3865, we additionally obtain [O II] λ 3727, H β , and [O III] λ λ 4959, 5007 emission lines. Combined with the H α -detection, a full suite of prominent rest-frame optical nebular lines are thus obtained for this object. We note that the [O II] flux may be underestimated due to the possible flux loss caused by the guiding drift issue known to NIRSPEC. Since CDFS-3865 was observed with NIRSPEC without any alignment star simultaneously, the maximum flux loss caused by the guiding drift ($\sim 1''.5$ per hour; private communication with NIRSPEC support scientists) could be comparable to the observed value. However, we do not know the drift direction, and the true flux loss cannot be estimated. Therefore, we do not correct for any flux loss for [O II]. We emphasize that the possible factor $\lesssim 2$ uncertainties in [O II] flux do not change our main results (§4.3). For COSMOS-30679, we obtain [O II] and [O III] λ 5007 emission lines, while we do not identify H β and [O III] λ 4959, because they fall in a dense OH-line wavelength range. We thus cannot place meaningful upper limits on their fluxes. When fluxes for these lines are required for inferring physical properties, we assume a value of 0.28 for the [O III] λ 4959/5007 ratio (e.g., Richard et al. 2011) and calculate the H β flux based on the observed H α flux, the intrinsic H α /H β ratio assuming Case B recombination (2.86; Osterbrock 1989), and the dust extinction estimated from SED fitting. We have checked for CDFS-3865 that the H β flux estimated in this way is consistent with the really observed H β flux (see also §4.2). We emphasize that the two LAEs, CDFS-3865 and COSMOS-30679, are the first [O II]-detected LAEs individually at high- z . The [O II]+[O III] lines provide the simultaneous determinations of ionization state and oxygen abundance (§4.3).

For CDFS-6482 and SSA22-8043, we detect [O III] λ 5007 while we do not identify H β and [O III] λ 4959, probably due to the contamination by OH-lines and the limited sensitivity of the instrument (More detailed descriptions about the MMIRS objects are provided by Hashimoto et al. 2013). For COSMOS-43982, we clearly detect [N II] λ 6584 emission line, which is not identified

TABLE 3
BROADBAND PHOTOMETRY OF THE LAES

COSMOS sample ⁽¹⁾	<i>B</i>	<i>V</i>	<i>r'</i>	<i>i'</i>	<i>z'</i>	<i>J</i>	...	<i>K_s</i>	[3.6]	[4.5]	[5.8]	[8.0]
COSMOS-08501	25.86	25.91	26.08	25.88	25.81	98.45	...	25.64	99.99	99.99	99.99	99.99
COSMOS-13636	24.43	24.21	24.35	24.19	24.24	23.10	...	23.43	24.10	23.75	99.99	99.99
COSMOS-30679	24.05	23.12	22.91	22.46	22.33	21.15	...	21.82	22.12	22.57	99.99	23.06
COSMOS-30679 ^(†)	24.76	23.82	24.44	24.09	23.49	22.31	...	23.29
COSMOS-43982	25.00	24.38	24.48	23.99	23.73	21.89	...	21.62	21.20	21.02	20.69	20.75
(limitmag)	(29.13)	(28.18)	(28.33)	(27.87)	(26.89)	(24.17)	...	(24.84)	(25.05)	(24.25)	(21.90)	(20.63)
(limitmag) ^(†)	(28.76)	(26.24)	(25.79)	(25.34)	(24.85)	(23.68)	...	(24.63)
CDFS sample ⁽²⁾	<i>B</i>	<i>V</i>	<i>R</i>	<i>I</i>	<i>z'</i>	<i>J</i>	<i>H</i>	<i>K</i>	[3.6]	[4.5]	[5.8]	[8.0]
CDFS-3865	23.01	22.94	22.92	23.14	22.93	22.73	22.27	22.38	22.82	22.82	22.51	23.00
CDFS-6482	23.93	23.87	23.78	23.95	23.67	23.50	23.36	23.07	22.88	22.83	22.34	99.99
(limitmag)	(28.32)	(27.85)	(27.82)	(26.14)	(25.64)	(24.57)	(24.57)	(23.97)	(26.23)	(25.68)	(23.66)	(23.43)
SSA22 sample ⁽³⁾	<i>B</i>	<i>V</i>	<i>R</i>	<i>i'</i>	<i>z'</i>	<i>J</i>	...	<i>K</i>	[3.6]	[4.5]	[5.8]	[8.0]
SSA22-8043	24.80	24.63	25.54	24.64	24.59	24.10	...	21.79	23.33	23.14	26.58	21.15
(limitmag)	(27.85)	(27.99)	(28.03)	(27.75)	(27.16)	(24.74)	...	(22.78)	(25.40)	(23.64)	(22.71)	(20.95)

NOTE. — Broadband photometry of the LAEs. All magnitudes are total magnitudes. 99.99 mag means no signal detected. Magnitudes in parentheses are 1σ uncertainties adopted in SED fitting.

⁽¹⁾ *BVR'i'z'* data are obtained from Subaru/Suprime-Cam, *J* data from UKIRT/WFCAM, *K_s* data from CFHT/WIRCAM, and [3.6] – [8.0] data from Spitzer/IRAC. All data are collected from the COSMOS Archive.

⁽²⁾ *BVRI* data are obtained from MPG/ESO 2.2m/WFI, *z'* data from CTIO/MOSAIC II, *JK* data from CTIO/ISPI, *H* data from NTT/SOFI, and [3.6] – [8.0] data from Spitzer/IRAC. Optical and NIR data are collected from the MUSYC Public Data Release (Gawiser et al. 2006), and Spitzer data from the SIMPLE Legacy II project.

⁽³⁾ *BVRIz'* data are obtained from Subaru/Suprime-Cam, *J* data from KPNO/NEWFIRM, *K* data from UKIRT/WFCAM, and [3.6] – [8.0] data from Spitzer/IRAC. Optical data are provided by T. Hayashino (see also Hayashino et al. 2004), *J* data are obtained from the NewH α survey (Ly et al. 2011; Lee et al. 2012). *K* data are collected from the WFCAM data access page, and Spitzer data from the Spitzer Heritage Archive.

^(†) Values obtained after removing the contribution from an adjacent object (§4.2). The limiting magnitudes are calculated by adding the photometric errors and additional errors (residuals after subtracting GALFIT models) in quadrature. The limiting magnitudes are thus shallower than those given above (photometric only).

for the other LAEs. The [N II]-detection suggests a non-negligible contribution of AGN to the emission lines for the object. Further investigations of AGN contamination are discussed in §4.1.

4. PHYSICAL PROPERTIES OF LAES

4.1. Removal of objects with AGN

AGN, as well as star-formation, can produce large amounts of ionizing photons, and show strong Ly α . Since our interest is star-forming LAEs, we need to remove LAEs with AGN activity from the sample.

During the LAE sample selection, bright LAEs with AGN signature have been removed (see Nakajima et al. 2012). Obvious AGNs are therefore excluded from the sample. However, the procedure is not always perfect, and can miss objects with relatively weak AGN activity. In order to assess possible contamination of AGN in our LAE sample, we plot our LAEs on a BPT diagram (Figure 3; Baldwin et al. 1981) which is widely used to separate star forming galaxies from AGN. In Figure 3, the underlying small gray points denote the spectroscopic objects from the Sloan Digital Sky Survey (SDSS; York et al. 2000)¹⁴. The two curves shown in Figure 3 are the empirical demarcations (Kewley et al. 2001; Kauffmann et al. 2003). Since only one LAE, CDFS-3865, has both [O III] and H β , all the other LAEs are shown with vertical lines. Due to the non-detection of [N II], the vertical lines show upper-limits of [N II]/H α except for COSMOS-43982, which has an individual [N II]

detection. Based on its relatively high [N II]/H α ratio, COSMOS-43982 may be contaminated by an AGN, though there remains a possibility that this LAE may be a star-formation dominated galaxy with a very small [O III]/H β ratio. For this analysis, we choose to be conservative and regard the object as a candidate possessing AGN activity. The properties of COSMOS-43982 are considered and interpreted carefully in the following sections.

For CDFS-3865, thanks to its relatively strong constraint on [N II]/H α , we can see that the object is along the star forming sequence and has negligible AGN activity, similar to two other LAEs with spectroscopic follow-up at similar redshifts (Finkelstein et al. 2011). Although the other LAEs have no constraint on their *y*-axis values, AGN contributions to them are assumed to be minimal, since there are few AGNs in the range $\log([\text{N II}]/\text{H}\alpha) \lesssim -0.5$, as suggested from the underlying SDSS galaxies. In order to check the assumption, we stack the *K* band spectra of the four NIRSPEC-detected LAEs¹⁵ with inverse-variance weights. The composite spectrum is shown in Figure 4, and provides an average, deeper constraint on [N II]/H α ratio for the LAEs. The red dot-dashed line in Figure 3 shows the upper-limit of [N II]/H α ratio constrained by the composite spectrum. The line is further away from the area occupied with AGNs. Therefore, AGN activity is on average negligible for the LAEs. In the following sections, we regard all the LAEs except for COSMOS-43982 as galaxies dominated by star-formation.

¹⁴ We use a part of the spectroscopic data taken from the MPA-JHU DR7 release of spectrum measurements: <http://www.mpa-garching.mpg.de/SDSS/DR7/>

¹⁵ We do not use the MMIRS spectra due to their worse sensitivity and spectral resolution.

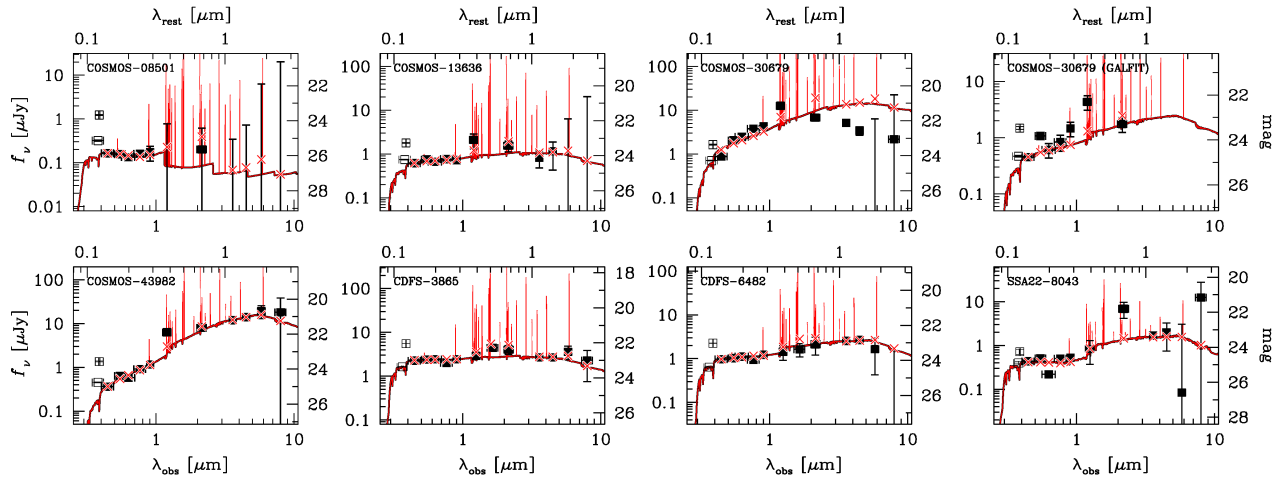


FIG. 5.— Results of SED fitting. The filled squares show the observed flux densities used for the fitting (B , V , r , i , z , J , (H) , K , [3.6], [4.5], [5.8], and [8.0]), while the open squares indicate those we omit for the fitting (U and NB387), due to the unknown flux contributions of IGM absorption. The red lines show the best-fit spectra, and the red crosses correspond to the best-fit flux densities.

TABLE 4
PHYSICAL PROPERTIES FROM SED FITTING

Object	$\log(M_*)$ (M_\odot)	$E(B-V)$ (mag)	$\log(\text{age})$ (yr)	$\log(\text{SFR})$ (M_\odot/yr)	χ^2
COSMOS-08501	$7.84^{+1.21}_{-0.27}$	$0.08^{+0.04}_{-0.08}$	$6.16^{+2.75}_{-1.06}$	$1.68^{+1.24}_{-1.44}$	1.825
COSMOS-13636	$9.12^{+0.13}_{-0.14}$	$0.18^{+0.01}_{-0.01}$	$7.34^{+0.23}_{-0.22}$	$1.80^{+0.08}_{-0.09}$	22.356
COSMOS-30679	$10.34^{+0.00}_{-0.00}$	$0.40^{+0.00}_{-0.00}$	$7.26^{+0.00}_{-0.00}$	$3.10^{+0.00}_{-0.00}$	7062.297
COSMOS-30679(†)	$9.74^{+0.26}_{-0.52}$	$0.24^{+0.04}_{-0.04}$	$8.01^{+0.45}_{-0.79}$	$1.79^{+0.29}_{-0.19}$	32.068
COSMOS-43982	$10.80^{+0.01}_{-0.06}$	$0.40^{+0.02}_{-0.01}$	$8.51^{+0.05}_{-0.15}$	$2.37^{+0.08}_{-0.04}$	71.642
CDFS-3865	$9.50^{+0.01}_{-0.03}$	$0.14^{+0.00}_{-0.00}$	$7.36^{+0.02}_{-0.04}$	$2.17^{+0.01}_{-0.01}$	32.170
CDFS-6482	$9.80^{+0.06}_{-0.05}$	$0.15^{+0.02}_{-0.02}$	$8.16^{+0.15}_{-0.15}$	$1.71^{+0.09}_{-0.09}$	12.374
SSA22-8043	$10.07^{+0.06}_{-0.06}$	$0.03^{+0.02}_{-0.01}$	$9.44^{+0.00}_{-0.10}$	$0.76^{+0.07}_{-0.03}$	112.288

NOTE. — Physical properties and their 1σ errors of LAEs from SED fitting. Stellar metallicity is fixed to $0.2 Z_\odot$. Escape fraction of ionizing photons is fixed to 0.05. (†) Values obtained after removing the contribution from an adjacent object (§4.2).

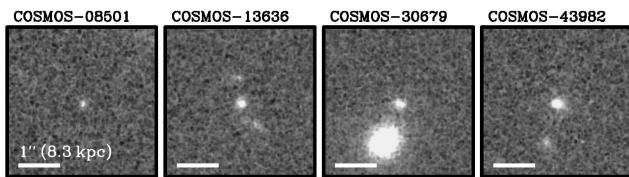


FIG. 6.— HST/ACS F814W images for COSMOS objects. White tick indicates 1 arcsec, corresponding to ~ 8.3 kpc at $z = 2.2$. North is up and east is to the left.

4.2. Stellar Mass and $E(B-V)$ from SED fitting

We perform SED fitting to broadband photometry to infer properties of the stellar populations. The majority of images are collected from publicly available databases (see notes in Table 3). The optical and NIR photometry is done with a $2''$ diameter aperture using the double-image mode of SExtractor (Bertin & Arnouts 1996). The aperture magnitudes are then converted into total magnitudes using aperture correction values, which are estimated from differences between aperture magnitudes and MAG_AUTO values for point sources. For the IRAC imaging, we use a $3''$ diameter aperture and Yan et al. (2005)’s aperture correction values. Table 3 summarizes the results.

The procedure of the SED fitting is the same as that

of Ono et al. (2010a), except for fixed redshifts, which are derived from $H\alpha$. Briefly, we use the stellar population synthesis model GALAXEV (Bruzual & Charlot 2003) for stellar SEDs, and include nebular emission (Schaerer & de Barros 2009). We set the escape fraction of ionizing photons ($f_{\text{esc}}^{\text{ion}}$) as 0.05. Such low $f_{\text{esc}}^{\text{ion}}$ has been suggested for $z \sim 3$ LBGs (e.g., Shapley et al. 2006; see also Iwata et al. 2009). Recently, Nestor et al. (2013) suggest that faint LAEs may have a higher $f_{\text{esc}}^{\text{ion}}$ (~ 0.10 – 0.30) in contrast with bright LBGs. We have checked that even if we assume $f_{\text{esc}}^{\text{ion}} = 0.20$, the derived quantities do not change significantly. We adopt a Salpeter initial mass function (IMF; Salpeter 1955) with lower and upper mass cut-offs of 0.1 and $100 M_\odot$. We choose constant star-formation history and the stellar metallicity $Z = 0.2 Z_\odot$. For dust extinction, we use Calzetti’s extinction law (Calzetti et al. 2000) on the assumption of $E(B-V)_{\text{gas}} = E(B-V)_*$ as proposed by Erb et al. (2006b), although this assumption is still debatable for high- z galaxies (e.g., Förster Schreiber et al. 2009; Ly et al. 2012)¹⁶. Intergalactic medium (IGM) at

¹⁶ Adopting $E(B-V)_{\text{gas}} = E(B-V)_*/0.44$ (Calzetti et al. 2000) decreases ionization parameters (§4.3) by a factor of $\lesssim 2$, but the changes are smaller than their 1σ errors. Changes in metallic-

TABLE 5
PHYSICAL PROPERTIES FROM THE NEBULAR LINES

Object	$12 + \log(\text{O}/\text{H})$		q_{ion} (10^7 cm s^{-1})	SFR ($M_{\odot} \text{ yr}^{-1}$)	SFR _{cor} ($M_{\odot} \text{ yr}^{-1}$)	EW(H α) (\AA)	$L(\text{H}\alpha)$ ($10^{42} \text{ erg s}^{-1}$)	EW(Ly α) (\AA)	$L(\text{Ly}\alpha)$ ($10^{42} \text{ erg s}^{-1}$)	AGN (10)
	N2 (1)	R23 (2)								
COSMOS-08501	< 8.73	$5.3^{+1.0}_{-1.0}$	$6.7^{+1.6}_{-2.1}$	> 280	0.67 ± 0.13	255 ± 26	8.41 ± 0.40	0
COSMOS-13636	< 8.61	$7.5^{+1.1}_{-1.1}$	$13.2^{+1.9}_{-1.9}$	93^{+26}_{-32}	0.95 ± 0.13	73 ± 5	11.35 ± 0.50	0
COSMOS-30679 ^(†)	< 8.46	$8.18^{+0.28}_{-0.28}$	8^{+10}_{-4}	$9.0^{+0.8}_{-0.8}$	$18.6^{+2.6}_{-2.6}$	93^{+25}_{-33}	1.14 ± 0.10	87 ± 7	8.47 ± 0.65	0
COSMOS-43982	$19.0^{+1.7}_{-1.7}$	$65.7^{+6.7}_{-6.0}$	41^{+4}_{-4}	2.41 ± 0.21	105 ± 8	11.00 ± 0.47	1
CDFS-3865	< 8.35	$7.84^{+0.24}_{-0.25}$	25^{+17}_{-8}	$107.9^{+6.7}_{-6.7}$	$166.0^{+10.3}_{-10.3}$	813^{+175}_{-216}	13.65 ± 0.85	64 ± 29	29.79 ± 4.93	0
CDFS-6482	< 8.72	$27.2^{+5.0}_{-5.0}$	$43.1^{+8.2}_{-8.2}$	261^{+103}_{-149}	3.45 ± 0.63	75 ± 52	15.40 ± 8.09	0
SSA22-8043	< 8.90	$41.0^{+12.0}_{-12.0}$	$44.4^{+13.2}_{-13.1}$	120^{+53}_{-69}	5.19 ± 1.52	28 ± 4	2.22 ± 0.38	0

NOTE. — (1) Oxygen abundance derived from N2-index (§4.3). If [N II] is undetected, 1σ upper-limit is given. (2) Oxygen abundance derived from R23-index (§4.3). Ionization parameter is derived at the same time. (3) Ionization parameter (10^7 cm s^{-1}) estimated from the [O III]/[O II] ratio and $Z(R23)$ (§4.3). (4) Star formation rate ($M_{\odot} \text{ yr}^{-1}$) derived from uncorrected H α luminosity (§4.4). (5) Star formation rate ($M_{\odot} \text{ yr}^{-1}$) derived from H α luminosity after correcting for extinction derived from SED fitting (§4.4). (6) Rest-frame equivalent width of H α (\AA ; §4.5). (7) Observed luminosity of H α ($10^{42} \text{ erg s}^{-1}$). (8) Rest-frame equivalent width of Ly α (\AA ; see Table §1). (9) Observed luminosity of Ly α ($10^{42} \text{ erg s}^{-1}$). (10) Flag of AGN (§4.1): AGN candidates are flagged with "1". (†) Values obtained after removing the contribution from an adjacent object (§4.2).

tenuation is calculated using the prescription given by Madau (1995). These assumptions are usually used for SED fitting for high- z LAEs. E.g., Guaita et al. (2011) test three different star-formation histories when performing SED fitting to $z \sim 2.1$ stacked LAEs, and find equally good fits to the data. The authors also note that SED fitting can relatively well constrain stellar mass and dust extinction among the free parameters. The derived properties are given in Table 4, and the best-fit SEDs are shown in Figure 5.

One problem is that COSMOS-30679 was found to be blended with another brighter adjacent object via examination of the COSMOS HST/ACS F814W imaging data (Figure 6). In order to deblend this object, we use the galaxy profile fitting software GALFIT (v3.0; Peng et al. 2010). We first run GALFIT in the B band and fit both objects simultaneously. Then, we perform fittings in other bands by fixing parameters (except for brightnesses) to those derived in the B band fitting and derive the deblended photometry, which is listed in Table 4. We confirm that the i' band brightness estimated from the deblended object is consistent with the photometry in the HST/ACS F814W high-resolution image within their errors. We add residuals after subtracting the fitted profiles into the photometric errors in quadrature, so that those errors are used in the SED fitting. Since the adjacent object appears dominant at longer wavelengths and deblending gets less reliable, we do not perform the deblending for the IRAC images. We therefore fit the SED of COSMOS-30679 after deblending without the IRAC data. The best fit SEDs of COSMOS-30679 after and before deblending are shown in upper right two panels in Figure 5. Although the bumpy shape of the SED after the deblending suggests additional contamination from the adjacent object, the fitting is acceptable (relatively small χ^2 value) compared with that obtained before deblending. In the following sections, we use the quantities after deblending.

We obtain from our sample stellar masses ranging from $7 \times 10^7 M_{\odot}$ to $1 \times 10^{10} M_{\odot}$ and dust extinction $E(B - V) = 0.03$ to 0.24 (except for the AGN LAE). These results are consistent with the previously recog-

inities are also small compared with the errors.

nized trend that LAEs at $z \sim 2$ are diverse, unlike higher redshift counterparts (e.g., Nilsson et al. 2011). We also find that dust extinctions estimated from the H α /H β ratio and SED fitting are consistent with each other for CDFS-3865 (Hashimoto et al. 2013). This supports our assumption that the dust extinction from SED fitting under the assumption of $E(B - V)_{\text{gas}} = E(B - V)_{\star}$ can be reasonably applied for the extinction correction of nebular lines.

4.3. Ionization Parameter and Metallicity

The ionization state in an HII region is often characterized by the ionization parameter, q_{ion} ¹⁷, which is the ratio of the mean ionizing photon flux to the mean hydrogen atom density. Larger q_{ion} means the HII region is more highly ionized, probably achieved by a harder ionizing spectrum. Consequently, emission lines with higher ionization potentials are expected to be observed more strongly with increasing q_{ion} . In this sense, the ionization parameter is well determined using ratios of emission lines of different ionization stages of the same element, such as the [O III]/[O II] ratio (e.g., Kewley & Dopita 2002). However, the [O III]/[O II] ratio depends not only on ionization state but also on gas metallicity (Fig. 1 of Kewley & Dopita 2002). Since the gas temperature decreases as gas metallicity increases, the far infrared fine-structure cooling by doubly ionized species (i.e., O²⁺) becomes efficient when the gas metallicity is high (e.g., Charlot & Longhetti 2001; Dopita et al. 2000), resulting in a decrease of [O III] line in optical. Conversely, metallicity estimates using $R23$ -index (Pagel et al. 1979):

$$R23 = \frac{[\text{O II}]\lambda 3727 + [\text{O III}]\lambda\lambda 5007, 4959}{\text{H}\beta} \quad (1)$$

are affected by the ionization parameter to some extent (e.g., Kewley & Dopita 2002; Nagao et al. 2006). Therefore, we combine the [O III]/[O II] ratio and $R23$ -index (both corrected for dust extinction estimated from SED fitting) to estimate its ionization parameter and metallicity at the same time iteratively. We assume in this

¹⁷ We use the subscript "ion" for the ionization parameter to distinguish it from the q -parameter which stands for the effect of dust on Ly α compared with UV-continuum (§5.2.1).

section $f_{\text{esc}}^{\text{ion}} = 0$ for simplicity. The possible effect of non-zero escape fractions will be discussed in §5.1.1.

We describe the procedure for CDFS-3865 as an example. As an initial guess of metallicity, we use the empirical $R23$ indicator determined by local galaxies (Maiolino et al. 2008). We obtain two solutions $12 + \log(\text{O}/\text{H}) = 7.45_{-0.19}^{+0.24}$ and $8.66_{-0.26}^{+0.20}$. We then use another alternative indicator, $N2$ -index defined as $[\text{N II}]\lambda 6584/\text{H}\alpha$ (Maiolino et al. 2008). The upper-limit of $[\text{N II}]/\text{H}\alpha$ provides an upper-limit of metallicity $12 + \log(\text{O}/\text{H}) = 8.35$ (1σ), which removes the high-metallicity solution by $R23$ -index at the 2.5σ level. Therefore, the empirical relation yields the metallicity $12 + \log(\text{O}/\text{H}) = 7.45_{-0.19}^{+0.24}$. As the second step, we use this metallicity and the $[\text{O III}]/[\text{O II}]$ ratio to estimate its ionization parameter. Kewley & Dopita (2002) calculate the relations between $[\text{O III}]/[\text{O II}]$ ratio and ionization parameter with discrete values of metallicity. Among them, our initial guess of metallicity corresponds to their lowest metallicity ($\sim 0.09 Z_{\odot}$; Allende Prieto et al. 2001). By using the relation, we find that the high $[\text{O III}]/[\text{O II}]$ ratio can only be reproduced with ionization parameters as high as several times 10^8 cm s^{-1} . As the third step, we recalculate its metallicity from the Kewley & Dopita (2002)'s relation ($R23$ -index) for the ionization parameter $3 \times 10^8 \text{ cm s}^{-1}$, and obtain $12 + \log(\text{O}/\text{H}) = 7.84_{-0.25}^{+0.2418}$. Finally, we recalculate its ionization parameter based on the metallicity and Eq. (12) of Kewley & Dopita (2002)¹⁹, and obtain $q_{\text{ion}} = 2.5_{-0.8}^{+1.7} \times 10^8 \text{ cm s}^{-1}$. This is consistent with the assumed ionization parameter in the third step ($3 \times 10^8 \text{ cm s}^{-1}$). We check that further iterations do not change our final solutions. To summarize, CDFS-3865 has the ionization parameter $q_{\text{ion}} = 2.5_{-0.8}^{+1.7} \times 10^8 \text{ cm s}^{-1}$ and the metallicity $12 + \log(\text{O}/\text{H}) = 7.84_{-0.25}^{+0.24}$.

In the same manner, we estimate COSMOS-30679's ionization parameter and metallicity to be $q_{\text{ion}} = 8_{-4}^{+10} \times 10^7 \text{ cm s}^{-1}$ and $12 + \log(\text{O}/\text{H}) = 8.18_{-0.28}^{+0.28}$, respectively. Since COSMOS-30679 does not have $\text{H}\beta$, its strength is inferred from $\text{H}\alpha$ assuming the Case B and the dust extinction. In addition, its broadband SED is fitted after being deblended with the adjacent object (§4.2). Therefore, the object may possess larger uncertainties.

For the LAEs without $[\text{O II}]$, we estimate their metallicities by using the empirical $N2$ -index relation, and no constraint on ionization parameters is provided for them. The metallicities and the ionization parameters are summarized in Table 5.

4.4. SFR

The $\text{H}\alpha$ luminosity is thought to be the most reliable SFR indicator relative to those based on the rest-frame UV and optical spectral features. Indeed, it is proportional to the birth rate of massive stars as well as being relatively insensitive to dust extinction as compared with UV-continuum. We measure the SFR of the LAEs from

the $\text{H}\alpha$ luminosity using the relation (Kennicutt 1998):

$$\text{SFR} [M_{\odot} \text{ yr}^{-1}] = 7.9 \times 10^{-42} L(\text{H}\alpha) \text{ erg s}^{-1}. \quad (2)$$

In Table 5, we summarize the derived SFRs.

4.5. $\text{H}\alpha$ Equivalent Width

We calculate the $\text{H}\alpha$ equivalent width of an object from the $\text{H}\alpha$ flux divided by its continuum flux density derived from K band photometry. To estimate the proper continuum, however, we have to remove the contribution of the $\text{H}\alpha$ emission on the K band photometry. We follow the prescription given in the appendix of Guaita et al. (2010) (see also Finkelstein et al. 2011):

$$f_{\nu}(\text{H}\alpha) = R_T \times \frac{F(\text{H}\alpha)}{\int T_K(\lambda) \frac{c}{\lambda^2} d\lambda}, \quad (3)$$

where $f_{\nu}(\text{H}\alpha)$ is the amount of flux that $\text{H}\alpha$ line contributes to the K band photometry, $F(\text{H}\alpha)$ is the observed $\text{H}\alpha$ flux, R_T is the ratio between the filter transmission at $\lambda_{\text{H}\alpha}$ and the maximum of the K band transmission function, and $T_K(\lambda)$ is the K band filter transmission at a given wavelength. The flux estimated from the calculation is subtracted from the K band photometry. The corrections span from 0.05 (COSMOS-43982) to as much as 0.63 mag (CDFS-3865). Since COSMOS-08501 is not detected in the K band, we use the 1σ lower-limit of the K band photometry. We thus obtain an upper-limit of the continuum (correction > 0.26 mag), hence a lower-limit of the EW($\text{H}\alpha$) for COSMOS-08501. The derived EWs($\text{H}\alpha$) are listed in Table 5.

5. DISCUSSION

In this section, we discuss the physical properties of LAEs determined by this study in conjunction with Finkelstein et al. (2011) and Nakajima et al. (2012). In the first subsection, we make comparisons in terms of ionization parameter, metallicity, and SFR of LAEs at $z \sim 2$ as well as lower-redshifts, and other galaxies at similar redshifts such as LBGs. We then examine the implications. In the second subsection, we show the properties of LAEs newly found by spectroscopy based on $\text{Ly}\alpha$ and $\text{H}\alpha$ hydrogen recombination lines. We extend the discussion to understanding the origins of the strong $\text{Ly}\alpha$ emission observed in LAEs.

5.1. Comparisons between LAEs and other galaxies

5.1.1. Ionization State

We find high ionization parameters for the LAEs. In this section, we examine this point further by comparison to other galaxies, and discuss its implications.

The situation is most clearly seen in Figure 7, which shows the $[\text{O III}]/[\text{O II}]$ ratio versus $R23$ -index. We plot CDFS-3865 and COSMOS-30679 (red circles), and other galaxies such as LBGs at $z = 2-3$ (blue symbols). The black grid represents model predictions of $[\text{O III}]/[\text{O II}]$ ratio and $R23$ -index at a given metallicity and (discrete) ionization parameter (Kewley & Dopita 2002). According to the calculation, CDFS-3865 is close to the $q_{\text{ion}} = 3 \times 10^8 \text{ cm s}^{-1}$ curve. This confirms its high ionization parameter and low oxygen abundance. The high ionization parameter is suggestive of CDFS-3865 showing a very hard ionizing spectrum. Therefore, one of the

¹⁸ Using the $1.5 \times 10^8 \text{ cm s}^{-1}$ relation does not change the metallicity estimate significantly (~ 0.02 dex lower).

¹⁹ Although the original relations are suspended at $q_{\text{ion}} = 3 \times 10^8 \text{ cm s}^{-1}$, we extend their polynomials toward higher q_{ion} values.

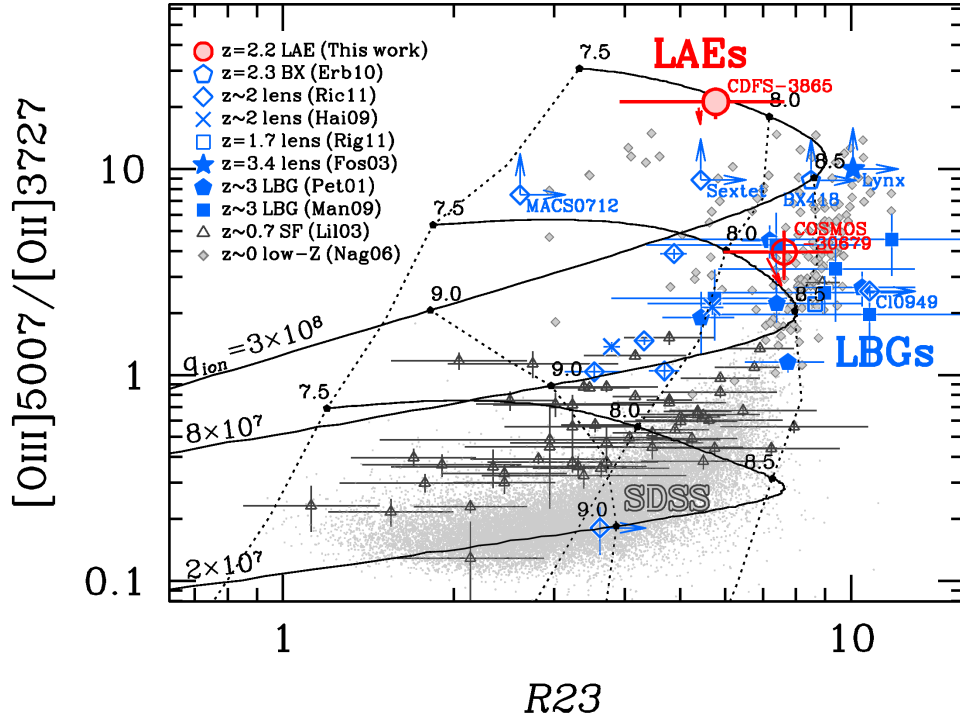


FIG. 7.— The emission line flux ratio $[O\text{ III}]\lambda 5007/[O\text{ II}]\lambda 3727$ vs. $R23$ -index for our $z = 2.2$ LAEs (CDFFS-3865: the solid red circle, COSMOS-30679: the open red circle) and non-LAEs (the blue symbols); the metal-poor BX galaxy at $z = 2.3$ (Erb et al. 2010: the open pentagon), lensed galaxies at $z \sim 2$ (Hainline et al. 2009: the crosses, Richard et al. 2011: the open diamonds, Rigby et al. 2011: the open square), the lensed galaxy at $z = 3.4$ (Fosbury et al. 2003: the solid star), $z \sim 3$ LBGs (Pettini et al. 2001: the solid pentagons, Mannucci et al. 2009: the solid squares), as well as the star forming galaxies at $0.47 < z < 0.92$ (Lilly et al. 2003: the black open triangles), and local star forming galaxies in the low-metallicity range ($7 \lesssim 12 + \log(O/H) \lesssim 8.5$: the gray diamonds) and high-metallicity range ($12 + \log(O/H) \gtrsim 8.2$: the gray dots) compiled by Nagao et al. (2006). The values on this plot are not corrected for dust extinction, except for the Nagao et al. (2006)'s local data points. For CDFFS-3865 and COSMOS-30679, effects of their extinction corrections are indicated by the red small arrows. The black grid shows photo-ionization model calculations (Kewley & Dopita 2002). For reference, the relations of $q_{ion} = 3 \times 10^8$, 8×10^7 , and $2 \times 10^7 \text{ cm s}^{-1}$ are shown, linked to each other at same metallicities, which are denoted by $12 + \log(O/H)$ values with dots.

most straightforward interpretations is that CDFFS-3865 is a young galaxy dominated by massive stars in possibly small star-forming regions (expected for young HII regions). Its low metallicity ($Z \sim 0.1 Z_{\odot}$) and large $EW(H\alpha)$ ($\sim 800 \text{ \AA}$) also support this idea (see also §5.1.2). The idea of LAEs being less-evolved galaxies is consistent with previous photometric results, such as low stellar masses (e.g., Pirzkal et al. 2007; Ono et al. 2010b) and small sizes (e.g., Bond et al. 2009; Malhotra et al. 2012).

Compared to CDFFS-3865, most other $z = 2-3$ galaxies appear to have lower ionization parameters. Notable exceptions are objects found by Fosbury et al. (2003), Erb et al. (2010), and (partly) Richard et al. (2011). Fosbury et al. (2003) and Erb et al. (2010) reveal from their multi-emission lines analysis that their galaxies possess high ionization parameters ($q_{ion} \gtrsim 10^9 \text{ cm s}^{-1}$), low metallicities ($Z \sim 0.1 Z_{\odot}$ or less), being roughly comparable to (or more or less extreme than) those found in CDFFS-3865. Interestingly, both galaxies turn out to exhibit strong $Ly\alpha$ emission. This supports our suggestion that strong $Ly\alpha$ galaxies are in part represented by young galaxies. Richard et al. (2011) also find two lensed galaxies (blue diamonds with upward arrow) possibly have high ionization parameters ($q_{ion} \gtrsim 10^8 \text{ cm s}^{-1}$) judged from their metallicities determined empirically ($12 + \log(O/H) = 8.00^{+0.44}_{-0.50}$ and $8.77^{+0.14}_{-0.14}$, for Sextet and

MACS0712, respectively). Unfortunately, $Ly\alpha$ measurements are not given in Richard et al. (2011).

However, as indicated by COSMOS-30679, LAEs' ionization parameters are unlikely to be always very high. The ionization parameter for COSMOS-30679 is estimated to be $q_{ion} = 8^{+10}_{-4} \times 10^7 \text{ cm s}^{-1}$, relatively high but comparable to those found in other high- z galaxies (e.g., Hainline et al. 2009) or LBGs (e.g., Mannucci et al. 2009), although the error is very large. COSMOS-30679 is thus considered to be more evolved than CDFFS-3865, suggested from its relatively higher metallicity, smaller $EW(H\alpha)$, older age estimated from SED fitting, and smaller ionization parameter.

Next, we compare our LAEs with galaxies seen in the local universe. In Figure 7, the gray dots indicate SDSS galaxies with $12 + \log(O/H) \gtrsim 8.2$ (Tremonti et al. 2004; Kewley & Dopita 2002) whose metallicities are derived by applying photoionization models to the most prominent optical emission lines ($[O\text{ II}]$, $H\beta$, $[O\text{ III}]$, $H\alpha$, $[N\text{ II}]$, $[S\text{ II}]$). They thus represent typical local galaxies. According to Dopita et al. (2006), the SDSS galaxies have ionization parameters $q_{ion} = \text{several} \times 10^7 \text{ cm s}^{-1}$ on average. Galaxies at $z = 2-3$ including the LAEs appear to have systematically higher ionization parameters than the SDSS galaxies. Galaxies at intermediate redshift ($z \sim 0.7$; Lilly et al. 2003) are also plotted in Figure 7. They appear to fall between $z \gtrsim 2$ galaxies

and the SDSS galaxies in Figure 7, showing systematically higher $[\text{O III}]/[\text{O II}]$ ratios than the SDSS galaxies. Since their metallicities are comparable to those of the SDSS galaxies (Lilly et al. 2003; Tremonti et al. 2004), the higher $[\text{O III}]/[\text{O II}]$ ratios are likely due to their somewhat higher ionization parameters. Combined with the findings of much higher $[\text{O III}]/[\text{O II}]$ ratios in $z = 2\text{--}3$ galaxies, higher- z galaxies tend to have higher ionization parameters.

Another interesting comparison is with the low-metallicity galaxies in the local universe. The gray diamonds in Figure 7 show local low-metallicity galaxies with $7 \lesssim 12 + \log(\text{O}/\text{H}) \lesssim 8.5$ (Nagao et al. 2006) whose metallicities are measured with the *direct* T_e method (e.g., Izotov et al. 2006). Unlike typical SDSS galaxies, they appear in almost the same parameter space occupied by high- z galaxies on Figure 7. Since their low-metallicities are determined by the *direct* T_e method and thus reliable, the high $[\text{O III}]/[\text{O II}]$ ratios can be interpreted as due to high ionization parameters. Indeed, from the comparison between $[\text{O III}]/[\text{O II}]$ ratios and photo-ionization models given in Nagao et al. (2006), it is inferred that local low-metallicity galaxies typically have higher ionization parameters ($\sim 8 \times 10^7 \text{ cm s}^{-1}$, or higher) than more metal-rich galaxies seen in the SDSS sample. Therefore, these low-metallicity galaxies in the local universe appear to have similar metallicities and ionization parameters as high- z star-forming galaxies including LBGs, and particularly those with extreme quantities are likely analogs of high- z LAEs such as CDFS-3865 in terms of their high ionization parameters and low metallicities.

One such extreme population is star-forming luminous compact galaxies (LCGs), or popularly referred to as “green pea” galaxies (GPs; Cardamone et al. 2009). The GPs are found in the SDSS spectroscopic sample²⁰ to have green colors in the SDSS *gri* composite images, caused by the very strong $[\text{O III}]$ emission lines with EWs of $\sim 1000 \text{ \AA}$ falling into the *r* band. They show low metallicities ($Z \sim 0.2 Z_\odot$; Amorín et al. 2010) and high ionization parameters ($\gtrsim 10^8 \text{ cm s}^{-1}$) inferred from their high $[\text{O III}]/[\text{O II}]$ ratios (Jaskot & Oey 2013), analogous to those observed in the LAEs. Their SFRs are also comparable to those for LAEs (Izotov et al. 2011), in contrast with more modest SFRs seen in typical local low-metallicity galaxies (e.g., Lee et al. 2004). A similar discussion is also provided by Xia et al. (2012).

In the SDSS Data Release 7 (DR7) spectroscopic galaxy sample, 251 GPs are found (Cardamone et al. 2009). Searching the entire SDSS DR7 spectroscopic sample yields 418,429 objects which fall in the GPs redshift range ($z = 0.112\text{--}0.360$; Cardamone et al. 2009) and are classified as GALAXY. Therefore, the GPs occupy only $\sim 0.06\%$ of the SDSS galaxy sample. Based on the luminosity function determined for the SDSS galaxies (Blanton et al. 2003), the number density is $\sim 1.5 \times 10^{-2} \text{ Mpc}^{-3}$ above a detection limit $M_r = -17.63$, which corresponds to $0.037 L^*$. The limit is calculated from the apparent magnitude limit ($r < 17.77$; Tremonti et al. 2004) for the spectroscopic sample and

the redshift threshold ($z > 0.028$; Nagao et al. 2006). The number density of the GPs is thus approximately $9 \times 10^{-6} \text{ Mpc}^{-3}$, which is almost consistent with the number density found by Cardamone et al. (2009) (~ 2 GPs per deg^2). On the other hand, the number density of LAEs at $z = 2.2$ is $\sim 1.7 \times 10^{-3} \text{ Mpc}^{-3}$ calculated by integrating the luminosity function provided by Hayes et al. (2010)²¹ above $L = 0.037 L^*$. The number density of the GPs is thus almost two order of magnitude smaller than that of LAEs. Therefore, if the GPs alone represent galaxies with high ionization parameter in the local universe, although it is still uncertain, the large difference of abundances between LAEs and the GPs suggests that such galaxies appear to be much more abundant at high- z while rarely seen in the local universe.

The final noteworthy implication of the high ionization parameters found in high- z LAEs is that such galaxies may provide additional photons that cause hydrogen reionization of the IGM in the early universe. Previous censuses of early galaxies have revealed a possible shortage of ionizing photons for the cosmic reionization (e.g., Ouchi et al. 2009; Robertson et al. 2010). Ouchi et al. (2009) find that the universe could not be totally ionized by only galaxies at $z = 7$ if there is no evolution of properties (e.g., escape fraction of ionizing photons ($f_{\text{esc}}^{\text{ion}}$), metallicity, dust extinction) from $z \sim 3$ to $z = 7$. One approach to resolve the problem is to adopt larger $f_{\text{esc}}^{\text{ion}}$, which may be the case for galaxies with higher ionization parameter. Since lower ionization species such as $[\text{O II}]$ dominate in the outer regions of an usual, ionization-bounded HII region (e.g., Shields 1990; Oey & Kennicutt 1997), a density-bounded HII region will show a larger $[\text{O III}]/[\text{O II}]$ ratio. Therefore, an ionization parameter depends not only on the hardness of the ionization radiation field but on the optical depth in an HII region (e.g., Brinchmann et al. 2008; Giammanco et al. 2005); higher ionization parameters are expected to be observed from optically thin, density-bounded HII regions. E.g., Giammanco et al. (2005) calculate that in the condition of density bounding, an HII region with $f_{\text{esc}}^{\text{ion}}=0.5$ shows the same ionization parameter as a region with $\sim \times 10$ greater ionizing flux without any photon escape. Consequently, the high ionization parameters found in the LAEs may be due to a low optical depth and a high $f_{\text{esc}}^{\text{ion}}$, probably achieved by density-bounded HII regions.

Although exact geometries of HII regions in LAEs are still uncertain, the LAE’s optically thin property has been suggested by recent studies. E.g., Hashimoto et al. (2013) investigate the kinematics of the galaxy scale outflows for LAEs using both $\text{Ly}\alpha$ emission and strong metal absorption lines, finding a tendency that LAEs have smaller values of neutral hydrogen column density in contrast with LBGs. Theoretically, Yajima & Li (2012) also suggest a completely ionized, optically thin phase can exist for LAEs. Therefore, the high ionization parameters may suggest LAEs can possess higher $f_{\text{esc}}^{\text{ion}}$, in contrast with LBGs showing modest fractions of photon escape. This trend is roughly consistent with the findings by Iwata et al. (2009) that LAEs tend to show smaller observed ratios of non-ionizing UV to Lyman continuum flux density than LBGs, as well as with

²⁰ Hence some of the GPs overlap with the local low-metallicity galaxies plotted with the gray diamond on Figure 7.

²¹ The detection limit is $L = 2.8 \times 10^{41} \text{ erg s}^{-1}$ ($\sim 0.02 L^*$).

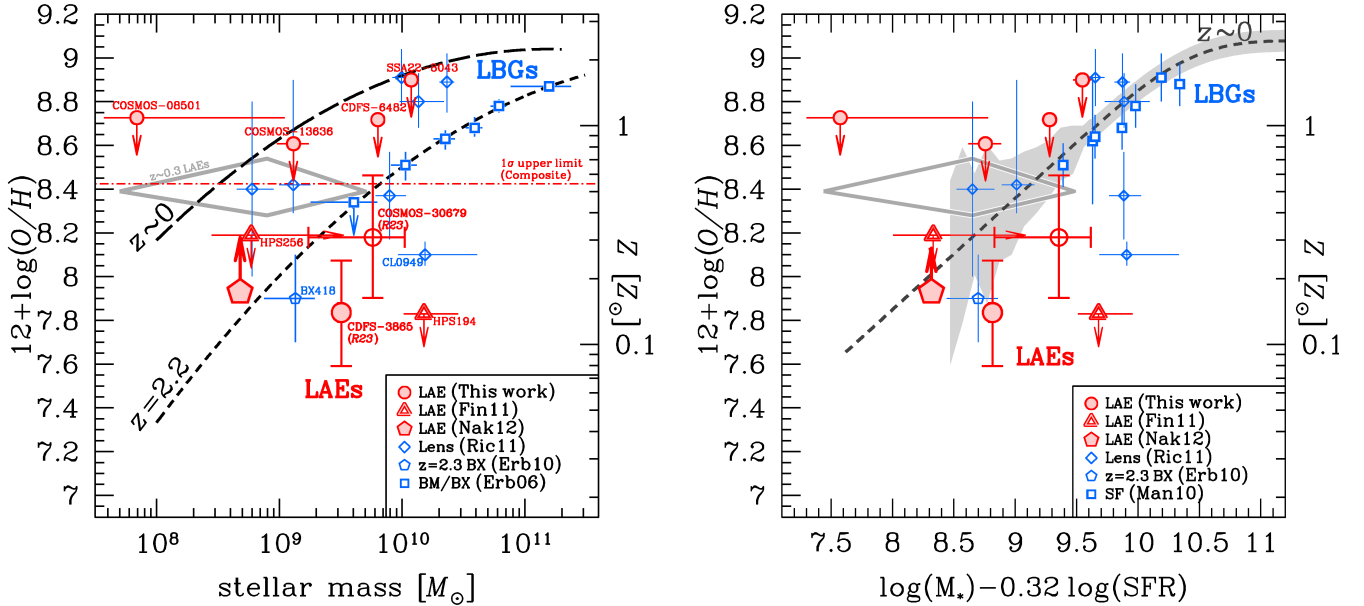


FIG. 8.— (left) Mass-metallicity (M-Z) relation for $z \sim 2$ LAEs (red symbols), lensed galaxies, and continuum selected galaxies (blue). The circles show our LAEs, whose metallicities are measured/constrained by using $R23$ -index (with error bar)/ $N2$ -index (1σ upper-limits). The red dot-dashed line shows the 1σ upper-limit of metallicity ($N2$ -index) for the composite spectrum in K band. We additionally plot the average LAE (pentagon: Nakajima et al. 2012) and two $z \sim 2.4$ LAEs (triangles: Finkelstein et al. 2011). LAEs at $z = 0.195 - 0.44$ are also shown with gray enclosed area (Cowie et al. 2011). For non-LAEs, we plot lensed galaxies at $1.5 < z < 2.5$ (open diamonds: Richard et al. 2011), the metal-poor BX galaxy at $z = 2.3$ (open pentagon: Erb et al. 2010), and BX/BM galaxies (open squares: Erb et al. 2006a). The M-Z relation compiled by Maiolino et al. (2008) at $z \sim 0$ and $z \sim 2$ are drawn as long-dashed and dashed curves, respectively. All data plotted here have been recalibrated to have the same metallicity scale (Maiolino et al. 2008) and IMF (Salpeter 1955) except for our LAEs with $R23$ -index whose metallicities are calibrated with Kewley & Dopita (2002)’s relations. (right) Fundamental metallicity relation proposed by Mannucci et al. (2010). The dashed curve and the shaded areas indicate the relation and its typical dispersions respectively, determined in the local universe (Mannucci et al. 2010, 2011). The open squares show $z \sim 2$ star forming galaxies collected/compiled by Mannucci et al. (2010) from Erb et al. (2006a) and so on. Other symbols are the same as those in the M-Z relation.

the latest measurements of $f_{\text{esc}}^{\text{ion}}$ s for both populations (Nestor et al. 2013). Similar suggestions of high escape fractions are also offered for LCGs, likely local analogs of high- z emission line galaxies (Jaskot & Oey 2013; Shim & Chary 2012). Since the fraction of LAEs among star-forming galaxies is known to increase with redshift (e.g., Ouchi et al. 2008; Stark et al. 2010), LAEs and similar low-mass galaxies could produce ionizing photons efficiently and play a key role in supplying ionizing photons for the cosmic reionization at $z \gtrsim 6$.

We note in conclusion that if the photon escapes are non-zero, LAEs’ ionizing fluxes need not necessarily to be as hard as we expect for zero escape fraction. A hard ionizing photon flux (young population), a high escape fraction of ionizing photons, or a combination of both conditions likely cause the high ionization parameters found in the LAEs.

5.1.2. Metallicity

Figure 8 (left) shows the observed mass-metallicity (M-Z) relation. The red symbols represent LAEs at $z \sim 2$, while the blue symbols show the other galaxies such as LBGs at the similar redshifts. Although some of our LAEs have just weak upper-limits of metallicity due to the lack of $[\text{N II}]$ -detection (§4.3), for CDFS-3865 and COSMOS-30679, we obtain the metallicity estimates from $R23$ -index with the oxygen lines. We plot these $R23$ metallicity estimates with larger circles in Figure 8. Albeit with its relatively large error in metallicity, CDFS-3865 falls below the conventional M-Z relation

of $z \sim 2$ LBGs. At least one LAE (HPS194) found by Finkelstein et al. (2011) also looks less chemically-enriched for its mass. Although the offsets of these LAEs from the M-Z relation can be due to the intrinsic scatter of the relation seen in the local universe (e.g., Tremonti et al. 2004), it may also indicate that they are less chemically evolved for their stellar masses. The idea is consistent with the suggestion of CDFS-3865’s high ionization parameters (e.g., BX418) tend to fall below the M-Z relation as well²², young galaxies with high ionization parameters may not follow the M-Z relation defined by more evolved galaxies. Unfortunately, no constraint on ionization parameter is given for HPS194. Alternatively, differences in star-formation activity may cause the scatter. We discuss this point later.

By contrast, the comparison with COSMOS-30679 is more unclear. Its large errors both in stellar mass and metallicity prevent us from telling if it is below/on the LBGs’ relation. Since its ionization parameter is comparable to those for LBGs (§5.1.1), COSMOS-30679 may be an LBG-like galaxy.

We also constrain an average metallicity from the K band composite spectrum (Figure 4) by using the empirical $[\text{N II}]$ -index. The 1σ (2σ) upper-limit of metallicity is $12 + \log(\text{O}/\text{H}) < 8.42$ (8.66), which corresponds

²² Galaxies with high ionization parameter (Fosbury et al. 2003; Richard et al. 2011) are omitted due to their high redshifts ($z > 2.5$). Since the M-Z relation is known to evolve with redshift, a direct comparison with the $z \sim 2$ LAEs is not appropriate.

to $Z < 0.54$ ($0.93 Z_{\odot}$). On the other hand, we independently obtain an average lower-limit of metallicity for LAEs to be $12 + \log(\text{O}/\text{H}) > 7.93$ (7.63), or $Z > 0.17$ ($0.09 Z_{\odot}$) at the 1σ (2σ) level, based on the $[\text{O II}]/(\text{H}\alpha + [\text{N II}])$ ratio whose fluxes are obtained by stacking 1.18 and $2.09 \mu\text{m}$ narrowband images for more than 100 LAEs (Nakajima et al. 2012). LAEs thus typically have a metallicity $12 + \log(\text{O}/\text{H}) = 7.93\text{--}8.42$ (7.63–8.66) at the 1σ (2σ) level. The range is robust in the sense that the upper-limit is constrained by bright, massive LAEs while the lower-limit by faint, low-mass LAEs. More spectroscopic data are needed, however, to conclude that there are no exceptional LAEs that have nearly zero or super-solar metallicities. The metallicity range also suggests that LAEs at $z \sim 2$ are rather less chemically enriched than those at $z \sim 0.3$ ($12 + \log(\text{O}/\text{H}) \sim 8.4^{23}$; Cowie et al. 2011).

Nakajima et al. (2012) find that LAEs fall typically above the M-Z relation below the stellar mass $\sim 10^9 M_{\odot}$. In contrast, the current study finds less chemically enriched LAEs for their masses. This apparent inconsistency may be due to the sampling of a large variety of evolutionary phases within the LAE population. Such variation has been indeed reported by other studies (e.g., Nilsson et al. 2011; Oteo et al. 2012). Alternatively, differences in star-formation activity may cause the inconsistency. To check the possibility, we plot the LAEs on the fundamental metallicity relation (FMR; Mannucci et al. 2010), the relation between stellar mass, metallicity, and SFR. In Figure 8 (right), most of the galaxies at $z = 0\text{--}2$ including the average LAE (Nakajima et al. 2012) appear to be consistent with the same FMR determined by the SDSS galaxies within their errors. However, some LAEs such as HPS194, and possibly CDFS-3865 and COSMOS-30679, still appear to fall below the relation. The inconsistency for HPS194 is remarkable ($\gtrsim 5\sigma$ level). Their low metallicities are not just likely due to their relatively high SFRs. We can speculate that the FMR is not universal and may fail to reproduce the properties of galaxies with e.g., high ionization parameter. Clearly however, much more data is needed to test the idea statistically.

5.1.3. Star-Formation Activity

In order to examine the star-formation activity of LAEs, we plot the LAEs on the sSFR versus stellar mass plane in Figure 9. We also plot BX/BM galaxies (Erb et al. 2006b) and sBzK galaxies (Hayashi et al. 2009). We note that this plot should be interpreted with care since the spectroscopic data introduce limits in the sensitivity to low SFRs.

BX/BM and sBzK galaxies follow a simple scaling relation between sSFR and the stellar mass, whose tight relation is referred to as *the star formation main sequence* (e.g., Daddi et al. 2007). Note that BX/BM and sBzK galaxies appear to have slightly different sequences; BX/BMs show lower sSFRs at a given mass. Compared to them, LAEs appear to follow the BX/BMs’ main sequence almost over the full mass range. CDFS-3865 and COSMOS-30679, which exhibit high ionization parameters and low metallicities, are not outliers on this

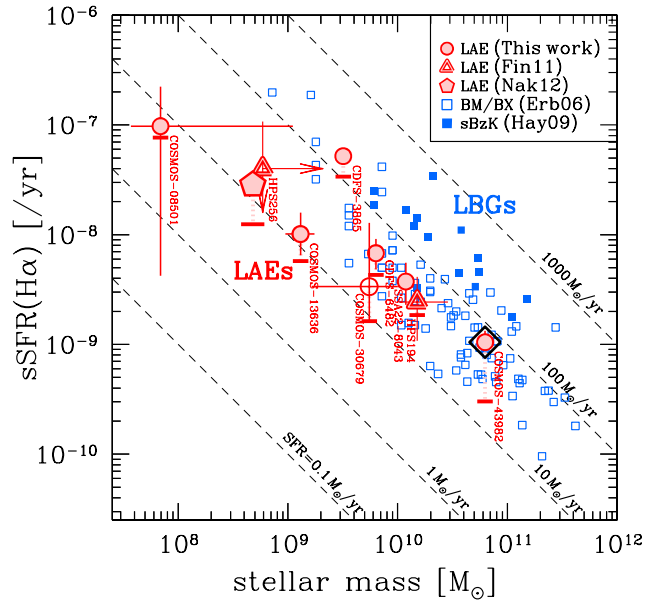


FIG. 9.— Relation between stellar mass and specific star formation rate (sSFR) for $z \sim 2$ LAEs (red) and continuum selected galaxies (blue); LAEs with NIR spectroscopy (circles: this work, triangles: Finkelstein et al. 2011), the average LAE obtained by stacking NIR NB imaging (pentagon: Nakajima et al. 2012), BX/BM galaxies (open squares: Erb et al. 2006b), and sBzK galaxies (solid squares: Hayashi et al. 2009). COSMOS-43982, a possible object with AGN activity, is marked with black diamond. The red open circle denotes COSMOS-30679, which has less accurate SED fitting results due to the neighbor’s contamination. All sSFRs plotted here are derived from $\text{H}\alpha$ luminosity with Salpeter IMF. The short horizontal bars in each symbol for the LAEs indicate the sSFR with no dust extinction correction. The dashed lines correspond to constant SFRs of 0.1, 1.0, 10, 100, and $1000 M_{\odot} \text{yr}^{-1}$.

diagram. This trend indicates that star-formation activities are well determined by their stellar mass, irrespective of the presence of $\text{Ly}\alpha$ emission. Interestingly, Rhoads et al. (2013) recently find that LAEs tend to have higher SFR surface densities for their gas mass surface densities than “normal” star-forming galaxies including BzK galaxies.

5.2. Physical Properties inferred from $\text{Ly}\alpha$ and $\text{H}\alpha$ emission

5.2.1. Correlation between $\text{EW}(\text{Ly}\alpha)$ and $\text{EW}(\text{H}\alpha)$

Figure 10 shows equivalent widths of $\text{Ly}\alpha$ and $\text{H}\alpha$ for LAEs (hereafter referred to as the “EWs diagram”). This plot may be useful to understand star-formation histories of LAEs, because the EWs’ continuum fluxes evolve in different ways when different star-formation histories are assumed. Another advantage of using the EWs is that both are pure observables and to zeroth order independent of dust extinction (the effect of dust will be discussed at the end of this section).

The superposed curves on Figure 10 illustrate evolutions of the EWs for the two extreme star-formation histories, instantaneous burst (dashed) and constant star-formation (solid) at several metallicities (Schaerer 2003)²⁴. For the instantaneous burst, since very massive stars ($M_{\star} \gtrsim 10 M_{\odot}$) complete their evolution within

²³ We recalculate the metallicity by using the Maiolino et al. (2008) indicator. The original estimate is ~ 0.15 dex lower.

²⁴ The models are collected from the Strasbourg astronomical Data Center (CDS). We present here the three metallicity cases assuming Salpeter IMF (Salpeter 1955) with upper (lower) mass

$\lesssim 10$ Myr, both EWs decline rapidly. As a result, their curves evolve quickly to lower-left on the EWs diagram. For the constant star-formation, on the other hand, the EW(Ly α) stops declining around ~ 100 Myr, because massive stars that are responsible for both Ly α emission and UV-continuum reach a steady mode. Since the EW(H α) keeps declining as the older stars build up in the galaxy, their slopes of the evolutionary tracks become less steep on the EWs diagram. Although Schaerer’s calculations stop at ~ 400 Myr for constant star-formation, the EW(Ly α) varies little after 100 Myr (Charlot & Fall 1993). Therefore, the tracks must extend to the left almost horizontally after the terminal points, reaching EW(H α) ~ 100 Å for the solar-metallicity case when an age of ~ 3 Gyr (e.g., Leitherer et al. 1999)²⁵.

Compared with the model tracks, some LAEs with EW(H α) ~ 1000 Å, CDFS-3865, HPS256 (Finkelstein et al. 2011), and possibly COSMOS-08501, can be explained by the instantaneous burst models with very young ages (a few Myr). The other LAEs whose EW(H α) is modest appear to prefer the constant star-formation models with $\gtrsim 100$ Myr. Although the sample is small, we find more than half of the LAEs appear to need a continuous star-formation history rather than an instantaneous burst.

Note, however, that since the EWs are sensitive to recent starbursts, LAEs on instantaneous tracks are not necessarily very young, but can be experiencing a burst after a continuous star-formation. Such a combination of burst plus continuous star-formation is indeed needed to explain the EWs of H α and optical colors observed in local dwarf galaxies (Lee 2006). An LAE with such a combined star-formation history will be on a track of instantaneous burst during starburst phases and on a track of constant star-formation for the remaining time.

Similarly, most of $z \sim 0.3$ LAEs appear to prefer continuous star-formation on the EWs diagram. Interestingly, $z \sim 2$ LAEs appear to have systematically higher EW(Ly α) and EW(H α) than lower- z LAEs. Although our spectroscopic sample may be biased toward larger EW(Ly α), the difference may be a sign that higher- z LAEs are younger. This idea is supported by the inference of lower metallicities at higher- z (§5.1.2; see also e.g., Finkelstein et al. 2009; Cowie et al. 2010, 2011).

However, one worry on the use of the EWs diagram is the effect of dust on Ly α . If the degree of dust extinction is different for Ly α and UV-continuum, EW(Ly α) is no longer independent of dust extinction. In order to examine this effect, we introduce a q parameter following Finkelstein et al. (2008). The q parameter is defined as $q = \tau(\text{Ly}\alpha)/\tau_{1216}$, where $\tau(\text{Ly}\alpha)$ and τ_{1216} are optical depth for Ly α and UV-continuum at $\lambda = 1216$ Å, respectively. Small q values (< 1) mean Ly α photons suffer less attenuation by dust than UV-continuum photons, while large values mean Ly α photons are more heavily attenuated.

cut-off to be $100 M_{\odot}$ ($1 M_{\odot}$). Case B recombination is assumed for an electron temperature of $T_e = 3 \times 10^4$ K at zero metallicity and $T_e = 10^4$ K otherwise, and an electron density of $n_e = 10^2 \text{ cm}^{-3}$.

²⁵ Although Leitherer et al. (1999) show the EW(H α) evolution with age until 1 Gyr, we extend the evolution toward older age smoothly to obtain EW(H α) ~ 100 Å at ~ 3 Gyr. We have confirmed the validity of the smooth extrapolation for constant star-formation by running GALAXEV (Bruzual & Charlot 2003).

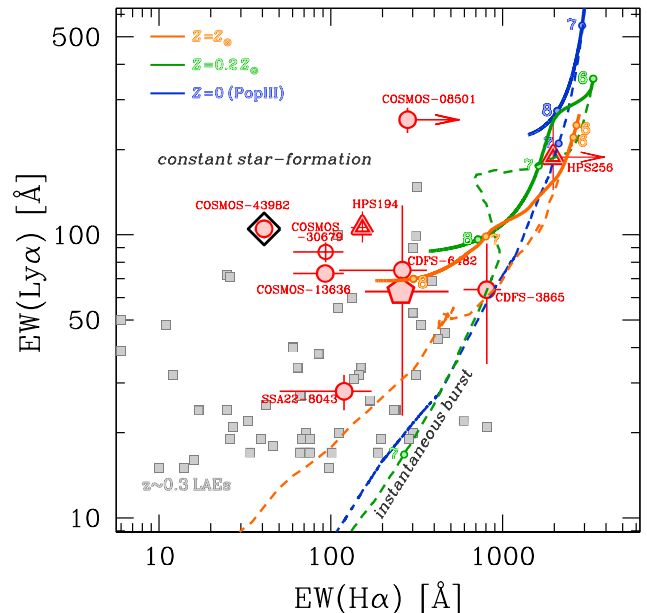


FIG. 10.— Relation between Ly α and H α equivalent widths. The red symbols show $z \sim 2$ LAEs (same as in Figure 9), and the gray squares show LAEs at $z = 0.3$ (Cowie et al. 2011). Superposed lines are evolutions of the EWs for instantaneous burst (dashed) and constant star-formation (solid) at metallicities of solar (orange), sub-solar (green), and zero (blue) calculated by Schaerer (2003). Ages are denoted by the numbers (6, 7, 8) near the dots on the lines which indicate (1 Myr, 10 Myr, 100 Myr). For the solar-metallicity models, the lower point labeled “6” is for the instantaneous burst.

ated. In the former (latter) case data points go down (up) on the EWs diagram after the corrections. From previous works, LAEs at $z \sim 2$ have modest q values; e.g., from the values given in Hayes et al. (2010) we calculate $q \simeq 1\text{--}1.5$ for $z = 2.2$ LAEs whose Ly α and H α luminosities are estimated from two narrowbands. Similarly, Nakajima et al. (2012) obtain $q = 0.7 \pm 0.1$. Blanc et al. (2011) obtain $q = 0.99$ for $z = 2\text{--}4$ LAEs whose intrinsic Ly α luminosities are inferred from UV-continuum. Therefore, LAEs are on average likely to show $q \sim 1$, and whose observed EWs(Ly α) to be approximately intrinsic. However, we find a non-negligible scatter in q -values around unity (especially toward smaller values) for the individual LAEs with H α measurement (§5.2.2; Figure 11 right). The LAEs with $q < 1$ go down on the EWs diagram and approach the instantaneous burst tracks. Unfortunately, with the current large errors in q -values, we cannot clearly tell which star-formation histories are likely for LAEs. Future radiative transfer calculations as well as higher S/N ratio spectra of Ly α and H α (and probably H β) will enable full use of the EWs diagram.

5.2.2. super Case B objects?

Figure 11 (left) shows the Ly α /H α ratio against EW(Ly α) for LAEs. The dark red symbols indicate the observed Ly α luminosity divided by the intrinsic H α luminosity corrected using the attenuation inferred from the SED fitting (i.e., showing lower-limits on the y -axis), while the light red symbols show the observed Ly α /H α ratios. A trend that LAEs with larger EW(Ly α) have larger Ly α /H α ratio appears to be present. This trend itself is not so surprising, but interestingly some LAEs, COSMOS-08501, and possibly COSMOS-13636 and one

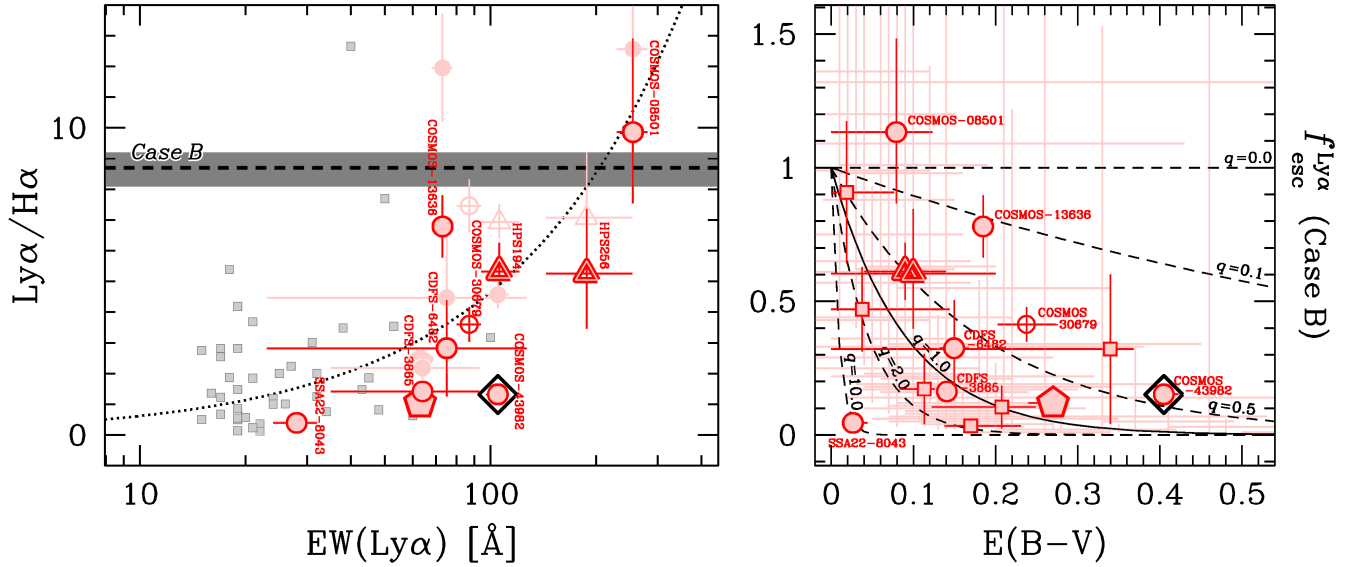


FIG. 11.— (left) $\text{Ly}\alpha/\text{H}\alpha$ flux ratio vs. $\text{EW}(\text{Ly}\alpha)$. Symbols are the same as in Figure 10. The darker symbols show the ratios calculated by the observed $\text{Ly}\alpha$ luminosity divided by the intrinsic $\text{H}\alpha$ luminosity (i.e., lower-limit of the ratios), while the lighter show the ratios calculated by the observed $\text{Ly}\alpha$ and $\text{H}\alpha$ luminosities. The ratios for $z \sim 0.3$ LAEs are based on observed luminosities. Dotted curve represents a single power-law fit given in Eq. (6). The dashed line and the gray shaded area show the $\text{Ly}\alpha/\text{H}\alpha$ ratio assuming the Case B recombination (8.7; Brocklehurst 1971) and its variation with electron density ($8.1\text{--}9.2$ with $n_e = 10^2\text{--}10^{10} \text{ cm}^{-3}$; Hummer & Storey 1987) when $T_e = 10^4 \text{ K}$, respectively. % (right) Escape fraction of $\text{Ly}\alpha$ photons (assuming the Case B) vs. dust extinction. The red squares show $z = 2.2$ LAEs (Hayes et al. 2010), and the faint-colored red error bars show $z = 2\text{--}4$ LAEs (Blanc et al. 2011). Superposed curves show the relations at a given q parameter ($q = 0.0, 0.1, 0.5, 1.0, 2.0, 10.0$).

LAE at $z \sim 0.3$, may have $\text{Ly}\alpha/\text{H}\alpha$ ratios exceeding the Case B recombination value (8.7; Brocklehurst 1971), which we call “super Case B”. Super Case B $\text{Ly}\alpha/\text{H}\alpha$ ratios have also been reported for some strong LAEs in the local universe (Hayes et al. 2007, Atek et al. 2008, Oti-Floranes et al. 2012, and references therein). The variation of the intrinsic $\text{Ly}\alpha/\text{H}\alpha$ ratio (the gray shaded area) does not seem to be a significant issue. Although it is not obvious that super Case B objects are really included in our sample due to their large errors, it is worth discussing possible physical origins of them in case they really exist.

We consider the possible effect of geometry, and the kinematics of dust and gas in the ISM. Neufeld (1991) propose a clumpy, multi-phase ISM where gas and dust are gathered in clouds within a low-density medium. With such circumstances, $\text{Ly}\alpha$ photons can be scattered at the surfaces of the clouds due to the resonant nature, while continuum photons would penetrate the clouds deeply. Since dust is contained in the clouds, $\text{Ly}\alpha$ photons would have a much smaller chance of encountering dust than other photons. In this scenario, a large $\text{EW}(\text{Ly}\alpha)$ and $\text{Ly}\alpha/\text{H}\alpha$ ratio can be observed. Alternatively, an outflow of the ISM can be a cause of strong $\text{Ly}\alpha$ emission (e.g., Kunth et al. 1998). However, Hashimoto et al. (2013) find an anti-correlation between $\text{EW}(\text{Ly}\alpha)$ and $\text{Ly}\alpha$ velocity offset for LAEs, the latter is considered to be positively correlated with outflow velocity. This anti-correlation is also supported by the observations of LBGs (Adelberger et al. 2003; see also Shapley et al. 2003; Pettini et al. 2001). In addition, the authors measure the LAEs’ outflow velocity directly from metal absorption lines, finding that outflow velocities for LAEs and LBGs are comparable. Therefore, outflows do not appear to be a major mechanism for producing large $\text{EW}(\text{Ly}\alpha)$ and $\text{Ly}\alpha/\text{H}\alpha$ ratio, though the sample

size of LAEs is still small and much more data as well as theoretical works to interpret the properties are needed.

In order to clarify the effects of a potentially clumpy geometry of ISM on $\text{Ly}\alpha/\text{H}\alpha$ ratios, we plot in Figure 11 (right) the relation between $E(B-V)$ and the escape fraction of $\text{Ly}\alpha$ photons ($f_{\text{esc}}^{\text{Ly}\alpha}$) under the Case B recombination assumption. We estimate $f_{\text{esc}}^{\text{Ly}\alpha}$ as

$$f_{\text{esc}}^{\text{Ly}\alpha} \equiv \frac{L_{\text{obs}}(\text{Ly}\alpha)}{L_{\text{int}}(\text{Ly}\alpha)} = \frac{L_{\text{obs}}(\text{Ly}\alpha)}{8.7L_{\text{int}}(\text{H}\alpha)}, \quad (4)$$

where subscripts ‘int’ and ‘obs’ refer to the intrinsic and observed quantities, respectively. The intrinsic $\text{H}\alpha$ luminosities are derived from the observed $\text{H}\alpha$ fluxes, corrected for dust extinctions. The superposed lines show the relations at a given q parameter (§5.2.1);

$$q = \frac{-\log(f_{\text{esc}}^{\text{Ly}\alpha})}{0.4k_{1216}E(B-V)}, \quad (5)$$

where k_{1216} is an extinction coefficient at $\lambda = 1216 \text{ \AA}$ (11.98; Calzetti et al. 2000). The clumpy geometry of ISM (or outflow) is favored by objects with $q = 0\text{--}1$. From Figure 11 (right), most of the LAEs presented here are located in the range $q = 0\text{--}1$; e.g., COSMOS-13636 and COSMOS-30679 have large $f_{\text{esc}}^{\text{Ly}\alpha}$ in spite of their moderate amounts of dust. SSA22-8043 has a large q parameter of ~ 10 , and can be an exception if its $\text{Ly}\alpha$ is heavily resonant-scattered by neutral hydrogen gas.

A notable object is COSMOS-08501. It appears to fall above the $q = 0$ line, where the clumpy ISM model does not work assuming Case B recombination, although the errors are relatively large. Moreover, since it is inferred to possess relatively small amount of dust, the large $\text{EW}(\text{Ly}\alpha)$ owing to the clumpy ISM is unlikely. In case the object is really super Case B, the only remaining explanation is the $\text{Ly}\alpha$ enhancement caused by collisional

excitations. Due to the decreasing collisional strengths with increasing principle quantum number, collisional excitations can lead to Ly α /H α ratios over the Case B value (see also Osterbrock 1989). Shocks caused by interactions with other sources, AGN activity, supernova explosions, strong outflows or infall are possible candidates for the collisional excitations.

Based on the HST images (Figure 6), COSMOS-08501, a super Case B candidate, looks very compact and shows no sign of interactions. COSMOS-13636, which has a very small q parameter, shows two faint sources nearby within ~ 5 kpc (projected) from the object. Its strong Ly α emission can be (partly) due to shocks caused by interactions. Indeed, some fractions of LAEs are turned out to exhibit morphologies suggestive of mergers at higher redshift (e.g., Pirzkal et al. 2007; Bond et al. 2009) as well as lower redshift (Cowie et al. 2010). Theoretically, Tilvi et al. (2011) demonstrate that mergers play an important role in mass assembly and star-formation in majority of the LAEs especially at higher redshift. Unfortunately, the shock-induced Ly α emission due to mergings has not yet been taken into account in these theoretical works (see also Tilvi et al. 2009). Alternatively, as discussed by Mori et al. (2004), supernova explosions can cause strong shocks, resulting in strong Ly α emission. Although the authors intend to explain extended Ly α blobs (~ 100 kpc) with high Ly α luminosities ($\sim 10^{43}$ erg s $^{-1}$), their basic ideas can be applied to normal LAEs. AGN activity and outflows seem unlikely (see §4.1 and Hashimoto et al. 2013).

When shocks (even partly) contribute to emission lines of LAEs, estimates of physical quantities such as ionization parameter (from [O III]/[O II] ratio), metallicity (from $N2$ -index), SFR (from H α), and dust extinction (from Balmer decrement) become less accurate. In particular, the intrinsic H α /H β value becomes larger when shocks are present, resulting in an overestimate of the abundance of dust. This effect may also help explain the presence of super Case B objects (e.g., Otí-Floranes et al. 2012). Thus, the results presented in this paper may require some corrections for the presence of shocks. We plan to address this in future work, through the simultaneous application of photo-ionization and shock models, with deeper spectroscopy which will detect the weaker lines not fully detected in the observations presented here (e.g., Balmer lines, [O II], [O III], [N II], [S II]).

A final remark is that from our discussions so far it is evident that Ly α is not a robust indicator of SFR for LAEs. The observed data ($z = 0-2$) in Figure 11 (left) are relatively well represented by a single power-law fit

$$\log(\text{Ly}\alpha/\text{H}\alpha)_{\text{obs}} = (-1.08 \pm 0.29) + (0.87 \pm 0.19) \times \log \text{EW}(\text{Ly}\alpha), \quad (6)$$

which is shown by the dotted curve in Figure 11 (left). According to this simple relation, SFRs of LAEs with $\text{EW}(\text{Ly}\alpha) \sim 20 \text{ \AA}$ (a typical threshold in narrowband searches) can be underestimated by a factor of about 10. Thus, SFRs estimated from Ly α may involve a factor of ~ 10 uncertainties intrinsically.

6. SUMMARY

We have presented NIRSPEC and MMIRS rest-frame optical spectra of seven Ly α emitters (LAEs) at $z =$

2.2, which are selected from our Subaru/Suprime-Cam NB387 survey in COSMOS, Chandra Deep Field South, and SSA22. Our first NIR spectroscopic result discusses the kinematics of LAEs and is presented in Hashimoto et al. (2013). As a companion study, this paper presents mainly the ionization and chemical properties of LAEs based on multiple nebular lines. Our sample includes one possibly AGN-dominated galaxy, and six star-forming galaxies. H α is detected in all six star-forming LAEs, while [N II] $\lambda 6584$ is only detected in the galaxy with signs of AGN activity. Among the six star-forming galaxies, one (CDF3-3865) also has detections of [O II] $\lambda 3727$, H β , and [O III] $\lambda\lambda 5007, 4959$, and another (COSMOS-30679) has detections of [O II] and [O III]. Our deep J band spectroscopic observations provide the first [O II]-detections for two individual LAEs at high- z . Our main results are summarized as follows.

- The [O III]/[O II] ratio vs. $R23$ -index diagram reveals that CDFS-3865 has a very high ionization parameter ($q_{\text{ion}} = 2.5_{-0.8}^{+1.7} \times 10^8 \text{ cm s}^{-1}$) and a low oxygen abundance (metallicity; $12 + \log(\text{O}/\text{H}) = 7.84_{-0.25}^{+0.24}$) in contrast with moderate values of other high- z galaxies such as LBGs. COSMOS-30679 also has a relatively high ionization parameter ($q_{\text{ion}} = 8_{-4}^{+10} \times 10^7 \text{ cm s}^{-1}$) and a low metallicity ($12 + \log(\text{O}/\text{H}) = 8.18_{-0.28}^{+0.28}$). LAEs would therefore 1) represent an early stage of galaxy formation dominated by massive stars in compact star-forming regions, and/or 2) have a higher escape fraction of ionizing photons probably achieved by density-bounded HII regions. High- q_{ion} galaxies like LAEs would thus play a key role in supplying ionizing photons for cosmic reionization in the early universe.
- Local low-metallicity galaxies ($7 \lesssim 12 + \log(\text{O}/\text{H}) \lesssim 8.5$) show similar ionization parameters and metallicities to high- z star-forming galaxies, and those with extreme quantities are likely analogs of high- z LAEs. One such population is “green pea” galaxies (GPs; Cardamone et al. 2009), in terms of their low-metallicity, high [O III]/[O II] ratios, and relatively high SFRs. A notable difference between the GPs and LAEs are their abundances; the GPs occupy only $\sim 0.06\%$ of the SDSS galaxy sample, and its number density is almost two order of magnitude smaller than that of LAEs at $z \sim 2$.
- CDFS-3865 falls below the mass-metallicity relation of LBGs at similar redshifts. Its low metallicity seems not to be explained by its star formation rate being taken into account, albeit with its relatively large error. COSMOS-30679 appears to exhibit the same trend, although its large error in metallicity complicates the interpretation. Interestingly, galaxies with high ionization parameters tend to fall below the relation. Such galaxies may not follow the relation determined by more evolved galaxies.
- The composite spectrum independently provides an upper-limit on the metallicity of $12 + \log(\text{O}/\text{H}) < 8.42$ (< 8.66) at the 1σ (2σ) level. Combined

with an lower-limit of metallicity (Nakajima et al. 2012), LAEs typically have metallicities $12 + \log(O/H) = 7.93\text{--}8.42$ (7.63–8.66) at the 1σ (2σ) level.

- In contrast to the large differences in ionization parameters and metallicity between LAEs and LBGs, we find LAEs have similar specific star formation rates as BX/BM galaxies at a given stellar mass.
- The EW(Ly α) vs. EW(H α) diagram interestingly suggests that more than half of the LAEs appear to need an extended star-formation such as a burst superimposed upon a continuous star-formation rather than the instantaneous burst alone. However, since EW(Ly α) may suffer from effects of dust and we do find a non-negligible scatter in q -values around unity (especially toward smaller values), we need to carefully interpret the result.
- LAEs with low q -values ($q = 0\text{--}1$) can be explained by the clumpy geometry of ISM. Interestingly, our sample may include objects with further enhanced Ly α , which we call super Case B. If they really exist, the only possible explanation is the collisional excitations of Ly α . Interactions with other sources and/or supernova explosions are possible key events that may cause shock-induced collisional excitation. If such shocks play a role in enhancement of the Ly α flux, physical quantities such as ionization parameter, metallicity, SFR, and dust

extinction should be re-computed using a combination of photo-ionization and shock-excitation models. We plan to investigate the role of shocks further in future works.

We are grateful to the staff of the W. M. Keck Observatory and Subaru telescope who keep the instruments and telescopes running effectively. Without their generous support, most of the observations presented here would not have been possible. We thank the referee, James E. Rhoads, for his many helpful comments and suggestions which greatly improved this paper. We also thank Tomohiro Yoshikawa and Masao Hayashi for their assistance with NIR spectroscopy data reduction, Tohru Nagao and Roberto Maiolino for providing the data of emission lines for local galaxies, Tomoki Hayashino for providing the imaging data in the SSA22 field, Matthew Hayes, Eros Vanzella, and Matthew Schenker for their helpful comments. The NewH α Survey team is thanked for providing their J band image of SSA22. This work was supported by World Premier International Research Center Initiative (WPI Initiative), MEXT, Japan, and KAKENHI (23244025) Grant-in-Aid for Scientific Research (A) through Japan Society for the Promotion of Science (JSPS). KN acknowledges support from the JSPS through JSPS research fellowships for Young Scientists.

Facilities: Keck II (NIRSPEC), Magellan:Clay (MMIRS), Subaru (Suprime-Cam)

REFERENCES

- Adelberger, K., Steidel, C. C., Shapley, A. E., & Pettini, M. 2003, *ApJ*, 584, 45
- Allende Prieto, C., Lambert, D. L., & Asplund, M. 2001, *ApJ*, 556, L63
- Amorín, R. O., Pérez-Montero, E., & Vílchez, J. M. 2010, *ApJ*, 715, L128
- Atek, H., Kunth, D., Hayes, M., Östlin, G., & Mas-Hesse, L. M. 2008, *A&A*, 488, 491
- Baldwin, J. A., Phillips, M. M., & Terlevich, R. 1981, *PASP*, 93, 5
- Bertin, E., & Arnouts, S. 1996, *A&AS*, 117, 393
- Blanc, G. A., et al. 2011, *ApJ*, 736, 31
- Blanton, M. R., et al. 2003, *ApJ*, 592, 819
- Bond, N. A., Gawiser, E., Gronwall, C., Ciardullo, R., Altmann, M., & Schawinski, K. 2009, *ApJ*, 705, 639
- Brinchmann, J., Pettini, M., & Charlot, S. 2008, *MNRAS*, 385, 769
- Brocklehurst, M. 1971, *MNRAS*, 153, 471
- Bruzual, G., & Charlot, S. 2003, *MNRAS*, 344, 1000
- Capak, P., et al. 2004, *AJ*, 127, 180
- Cardamone, C., et al. 2009, *MNRAS*, 399, 1199
- Calzetti, D., Armus, L., Bohlin, R. C., Kinney, A. L., Koornneef, J., & Storchi-Bergmann, T. 2000, *ApJ*, 533, 682
- Charlot, S., & Fall, S. M. 1993, *ApJ*, 415, 580
- Charlot, S., & Longhetti, M. 2001, *MNRAS*, 323, 887
- Cowie, L. L., & Hu, E. M. 1998, *AJ*, 115, 1319
- Cowie, L. L., Barger, A. J., & Hu, E. M. 2010, *ApJ*, 711, 928
- Cowie, L. L., Barger, A. J., & Hu, E. M. 2011, *ApJ*, 738, 136
- Daddi, E., et al. 2007, *ApJ*, 670, 156
- Dopita, M. A., Kewley, L. J., Heisler, C. A., & Sutherland, R. S. 2000, *ApJ*, 542, 224
- Dopita, M. A., et al. 2006, *ApJ*, 647, 244
- Erb, D. K., Shapley, A. E., Pettini, M., Steidel, C. C., Reddy, N. A., & Adelberger, K. L. 2006a, *ApJ*, 644, 813
- Erb, D. K., Steidel, C. C., Shapley, A. E., Pettini, M., Reddy, N. A., & Adelberger, K. L. 2006b, *ApJ*, 647, 128
- Erb, D. K., Pettini, M., Shapley, A. E., Steidel, C. C., Law, D. R., & Reddy, N. A. 2010, *ApJ*, 719, 1168
- Finkelstein, S. L., Rhoads, J. E., Malhotra, S., Grogin, N., & Wang, J. 2008, *ApJ*, 678, 655
- Finkelstein, S. L., Cohen, S. H., Malhotra, S., & Rhoads, J. E. 2009, *ApJ*, 700, 276
- Finkelstein, S. L., et al. 2011, *ApJ*, 729, 140
- Förster Schreiber, N. M., et al. 2009, *ApJ*, 706, 1364
- Fosbury, R. A. E., et al. 2003, *ApJ*, 506, 797
- Furusawa, H., et al. 2008, *ApJS*, 176, 1
- Gawiser, E., et al. 2006, *ApJ*, 642, L13
- Gawiser, E., et al. 2007, *ApJ*, 671, 278
- Giacconi, R., Rosati, P., Tozzi, P., et al. 2001, *ApJ*, 551, 624
- Giammanco, C., Beckman, J. E., & Cedrés, B. 2005, *A&A*, 438, 599
- Gray, R. O., & Corbally, C. J. 1994, *AJ*, 107, 742
- Gronwall, C., et al. 2007, *ApJ*, 667, 79
- Guaita, L., et al. 2010, *ApJ*, 714, 255
- Guaita, L., et al. 2011, *ApJ*, 733, 114
- Hainline, K. N., Sharpley, A. E., Kornei, K. A., Pettini, M., Buckley-Geer, E., Allam, S. S., & Tucker, D. L. 2009, *ApJ*, 701, 52
- Hashimoto, T., et al. 2013, *ApJ*, 765, 70
- Hayashi, M., et al. 2009, *ApJ*, 691, 140
- Hayashino, T., et al. 2004, *AJ*, 128, 2073
- Hayes, M., et al. 2007, *MNRAS*, 382, 1465
- Hayes, M., et al. 2010, *Nature*, 464, 562
- Hummer, D. G., & Storey, P. J. 1987, *MNRAS*, 224, 801
- Iwata, I., et al. 2009, *ApJ*, 692, 1287
- Izotov, Y. I., Stasińska, G., Meynet, G., Guseva, N. G., & Thuan, T. X. 2006, *A&A*, 448, 955
- Izotov, Y. I., Guseva, N. G., & Thuan, T. X. 2011, *ApJ*, 728, 161
- Jaskot, A. E., & Oey, M. S. 2013, *arXiv:1301.0530*
- Kauffmann, G., et al. 2003, *MNRAS*, 346, 1055
- Kennicutt, R. C., Jr. 1998, *ARA&A*, 36, 189
- Kewley, L. J., Dopita, M. A., Sutherland, R. S., Heisler, C. A., & Trevena, J. 2001, *ApJ*, 556, 121
- Kewley, L. J., & Dopita, M. A. 2002, *ApJS*, 142, 35

- Kunth, D., Mas-Hesse, J. M., Terlevich, E., Terlevich, R., Lequeux, J., & Fall, S. M. 1998, *A&A*, 334, 11
- Kurucz, R. 1993, Kurucz CD-ROM 13 (Cambridge, MA: SAO)
- Lee, J. C., Salzer, J. J., & Melbourne, J. 2004, *ApJ*, 616, 752
- Lee, J. C. 2006, PhD thesis, Univ. Arizona
- Lee, J. C., et al. 2012, arXiv:1205.0017
- Leitherer, C., et al. 1999, *ApJS*, 123, 3
- Lilly, S. J., Carollo, C. M., & Stockton, A. N. 2003, *ApJ*, 597, 730
- Ly, C., et al. 2011, *ApJ*, 726, 109
- Ly, C., Malkan, M. A., Kashikawa, N., Ota, K., Shimasaku, K., Iya, M., & Currie, T. 2012, *ApJ*, 747, L16
- Madau, P. 1995, *ApJ*, 441, 18
- Maiolino, R., et al. 2008, *A&A*, 488, 463
- Malhotra, S., & Rhoads, J. E. 2002, *ApJ*, 565, 71
- Malhotra, S., Rhoads, J. E., Finkelstein, S. L., Hathi, N., Nilsson, K., McLinden, E., & Pirzkal, N. 2012, *ApJ*, 750, L36
- Mannucci, F., et al. 2009, *MNRAS*, 398, 1915
- Mannucci, F., Cresci, G., Maiolino, R., Marconi, A., & Gnerucci, A. 2010, *MNRAS*, 408, 2115
- Mannucci, F., Salvaterra, R., & Campisi, M.A. 2011, *MNRAS*, 414, 1263
- McLinden, E. M., et al. 2011, *ApJ*, 730, 136
- Miyazaki, S., et al. 2002, *PASJ*, 54, 833
- Mori, M., Umemura, M., & Ferrara, A. 2004, *ApJ*, 613, L97
- Nagao, T., Maiolino, R., & Marconi, A. 2006, *A&A*, 459, 85
- Nakajima, K., et al. 2012, *ApJ*, 745, 12
- Nestor, D. B., Shapley, A. E., Kornei, K. A., Steidel, C. C., & Siana, B. 2013, *ApJ*, 765, 47
- Neufeld, D. A. 1991, *ApJ*, 370, L85
- Nilsson, K. K., et al. 2009, *A&A*, 498, 13
- Nilsson, K. K., Östlin, G., Møller, P., Möller-Nilsson, O., Tapken, C., Freudling, W., & Fynbo, J. P. U. 2011, *A&A*, 529, 9
- Nonino, M., et al. 2009, *ApJS*, 183, 244
- Oey, M. S., & Kennicutt, R. C., Jr. 1997, *MNRAS*, 291, 827
- Oke, J. B. 1974, *ApJS*, 27, 21
- Ono, Y., Ouchi, M., Shimasaku, K., Dunlop, J., Farrah, D., McLure, R., & Okamura, S. 2010a, *ApJ*, 724, 1524
- Ono, Y., et al. 2010b, *MNRAS*, 402, 1580
- Osterbrock, D. E. 1989, *Astrophysics of Gaseous Nebulae and Active Galactic Nuclei*. University Science Books, Suasalito, CA
- Oteo, I., et al. 2012, arXiv:1202.0997
- Otí-Flóranes, H., et al. 2012, arXiv:1207.7303
- Ouchi, M., et al. 2003, *ApJ*, 582, 60
- Ouchi, M., et al. 2008, *ApJS*, 176, 301
- Ouchi, M., et al. 2009, *ApJS*, 706, 1136
- Overzier, R. A., et al. 2008, *ApJ*, 673, 143
- Pagel, B. E. J., Edmunds, M. G., Blackwell, D. E., Chun, M. S., & Smith, G. 1979, *MNRAS*, 189, 95
- Peng, C. Y., Ho, L. C., Impey, C. D., & Rix, H. 2010, *AJ*, 139, 2097
- Pettini, M., et al. 2001, *ApJ*, 554, 981
- Pirzkal, N., Malhotra, S., Rhoads, J. E., & Xu, C. 2007, *ApJ*, 667, 49
- Rhoads, J. E., Malhotra, S., Finkelstein, S. L., Fynbo, J. P. U., McLinden, E. M., Richardson, M. L. A., & Tilvi, V., S. 2013, arXiv:1301.3140
- Richard, J., Jones, T., Ellis, R., Stark, D. P., Livermore, R., & Swinbank, M. 2011, *MNRAS*, 413, 643
- Rigby, J. R., Wuyts, E., Gladders, M. D., Sharon, K., & Becker, G. D. 2011, *ApJ*, 732, 59
- Rousselot, P., Lidman, C., Cuby, J. G., Moreels, G., & Monnet, G. 2000, *A&A*, 354, 1134
- Robertson, B. E., Ellis, R. S., Dunlop, J. S., McLure, R. J., & Stark, D. P. 2010, *Nature*, 468, 49
- Salpeter, E. E. 1955, *ApJ*, 121, 161
- Schaerer, D. 2003, *A&A*, 397, 527
- Schaerer, D. & de Barros, S. 2009, *A&A*, 502, 423
- Scoville, N., et al. 2007, *ApJS*, 172, 1
- Shapley, A. E., Steidel, C. C., Pettini, M., & Adelberger, K. L. 2003, *ApJ*, 588, 65
- Shapley, A. E., Steidel, C. C., Pettini, M., Adelberger, K. L., & Erb, D. K. 2006, *ApJ*, 651, 688
- Shields, G. A. 1990, *ARA&A*, 28, 525
- Shim, H., & Chary, R. R. 2012, arXiv:1205.0949
- Shimasaku, K., et al. 2006, *PASJ*, 58, 313
- Stark, D. P., Ellis, R. S., Chio, K., Ouchi, M., & Bunker, A. 2010, *MNRAS*, 408, 1628
- Steidel, C. C., Adelberger, K. L., Kurt L., Shapley, A. E., Pettini, M., Dickinson, M. & Giavalisco, M. 2000, *ApJ*, 532, 170
- Tilvi, V., Malhotra, S., Rhoads, J. E., Scannapieco, E., Thacker, R. J., Ilev, I. T., & Mellema, G. 2009, *ApJ*, 704, 724
- Tilvi, V., Scannapieco, E., Malhotra, S., & Rhoads, J. E. 2011, *MNRAS*, 418, 2196
- Tremonti, C. A., Heckman, T. M., Kauffmann, G., et al. 2004, *ApJ*, 613, 898
- van Dokkum, P. G. 2001, *PASP*, 113, 1420
- Venemans, B. P., et al. 2005, *A&A*, 431, 793
- Xia, L., et al. 2012, *AJ*, 144, 28
- Yajima, H., & Li, Y. 2012, arXiv:1211.0088
- Yan, H., et al. 2005, *ApJ*, 634, 109
- York, D. G., et al. 2000, *AJ*, 120, 1579
- Yoshikawa, T., et al. 2010, *ApJ*, 718, 112